International Journal of Mechanical Sciences 326 (2026) 111885

Contents lists available at ScienceDirect

International Journal of Mechanical Sciences

journal homepage: www.elsevier.com/locate/ijmecsci

Programming energy absorption via 4D-printed reconfigurable gradient metamaterials

Zhao Peng [a], Chengjun Zeng [a], Wei Zhao [a,*], Jinsong Leng [b], Yanju Liu [a,c,*]

[a] Department of Astronautical Science and Mechanics, Harbin Institute of Technology (HIT), No. 92 West Dazhi Street, PO Box 301, Harbin, 150001, People's Republic of China
[b] Center for Composite Materials and Structures, Harbin Institute of Technology (HIT), No. 2 YiKuang Street, Harbin, 150080, People's Republic of China
[c] Suzhou Research Institute, Harbin Institute of Technology, Suzhou, 215100, PR China

ARTICLE INFO

Keywords:
4D printing
Shape-memory
Programming
Reconfigurable
Gradient metamaterials
Energy absorption

ABSTRACT

Programmable energy-absorbing metamaterials that combine broad load regulation with reusability remain difficult to realize, because most existing architectures exhibit fixed post-fabrication responses and mainly provide a single dominant load plateau. In this study, a 4D-printed gradient corrugated plate-tube (CorTube) metamaterial is proposed by integrating gradient sequencing with shape-memory polylactic acid. Quasi-static compression experiments and finite-element simulations show that the gradient design transforms relatively concentrated collapse in homogeneous units into staged progressive collapse in the assembled structure, thereby generating separated load plateaus over a broader stress range. A mechanism-based interpretation further reveals that different gradient parameters play distinct roles in redistributing local activation events. The tube spacing mainly controls the onset and stability of the first plateau, the corrugation angle mainly governs the collapse sequence and plateau separation, and tube diameter serves mainly as a secondary tuning parameter. Among the tested designs, the angle-gradient CorTube exhibits the best overall performance, reaching a total specific energy absorption of 1.088 J/g, which is an 8-fold enhancement relative to the best homogeneous CorTube unit structure. Besides, it also generates two additional load plateaus at 4.76 and 10.72 MPa. The structure further recovers its original shape within 5 s at 80 °C after large deformation. And cyclic tests show that the linear regime and the first load plateau remain nearly unchanged throughout six compression cycles, exhibiting excellent repeatability. The second and third load plateaus are highly stable during the first three cycles but gradually degrade from the fourth cycle onward due to accumulated local damage. The structure fully recovers its original shape within 5 s at 80 °C, demonstrating reusable early-stage performance over six cycles and stable multi-plateau behavior for at least three cycles. Finally, a scaled UAV landing buffer prototype using four type2 CorTube units was designed and tested, confirming the engineering feasibility of multi-stage buffering and thermal reusability. These results demonstrate that combining gradient architecture with shape-memory reconfiguration provides an effective route to lightweight, multi-cycle reusable, and mechanically adaptive energy-absorbing metamaterials for protective and buffering applications.

1. Introduction

Mechanical metamaterials transcend the intrinsic limitations of their base materials by employing rationally engineered microstructural architectures [1–6]. Representative examples include honeycomb lattices, auxetic networks, and multistable systems, which have found widespread application in shock absorption, aerospace engineering, biomedical devices, and adaptive sensing technologies [7–15]. Advances in additive manufacturing have enabled the precise fabrication of complex metamaterial architectures across multiple length scales, opening new avenues for the realization of programmable and customizable mechanical performance [16–21].

Energy-absorbing mechanical metamaterials have garnered significant interest owing to their lightweight nature and their capacity to achieve efficient load redistribution via hierarchical structural organization [22]. Conventional designs, such as honeycomb lattices, auxetic

* Corresponding authors at: Department of Astronautical Science and Mechanics, Harbin Institute of Technology (HIT), No. 92 West Dazhi Street, PO Box 301, Harbin, 150001, People's Republic of China.
E-mail addresses: zhaowei123@hit.edu.cn (W. Zhao), yj_liu@hit.edu.cn (Y. Liu).

https://doi.org/10.1016/j.ijmecsci.2026.111885
Received 30 March 2026; Received in revised form 1 June 2026; Accepted 1 July 2026
Available online 8 July 2026

structures, and multistable systems, dissipate energy through well-controlled collapse mechanisms [23–28]. Minh-Son Pham et al. [29] develop robust and damage-resistant architectural materials by mimicking the microstructure of crystalline materials, such as grain boundaries, precipitates, and phases. Nevertheless, most existing metamaterials are constructed from uniform, periodically repeated units with fixed geometric parameters [30], resulting in static mechanical responses post-fabrication [31–33]. This inherent rigidity poses a major challenge in engineering applications, where spatially heterogeneous stress fields necessitate region-specific mechanical properties to optimize overall energy absorption [34–40]. For instance, personal protective equipment such as helmets must accommodate impacts of varying magnitudes to prevent neck injuries from "overprotection" and brain injuries from "underprotection" [41–45].

Biological gradient structures offer a compelling paradigm for addressing these challenges. For instance, the gradient helical microstructures observed in mantis shrimp (Stomatopoda) [46–49] and the radial distribution of vascular bundles in bamboo (Bambusoideae) [50–53] exemplify how spatial modulation of microstructural attributes, such as orientation, density, and geometry, can optimize performance under multiaxial loading conditions. Modular mechanical metamaterials, through flexible assembly, disassembly, and reassembly, enable on-demand tuning of mechanical responses to accommodate complex loading environments and evolving protection requirements [54–56]. Inspired by such natural and modular strategies, gradient composites have been successfully deployed in automotive [57,58], aerospace [59,60], and vibration mitigation systems [61,62]. Recent investigations further reveal that gradient approaches, such as unit cell parameter gradients and graded densification, can markedly enhance the energy absorption of metamaterials by strategically controlling collapse sequences and stress propagation pathways [63–66]. For example, Zhang et al. [67] increased the specific energy absorption of corrugated wall metamaterials by 30.6% via gradient optimization. Liu Haitao et al. [68] employed the CHSO gradient design to investigate the effects of the number of gradient layers and gradient distribution pattern on peak stress, plateau stress, and structural specific energy absorption. Nian et al. [69] introduced a new class of bio-inspired and 3D-printed metastructures with improved stiffness-to-weight ratio and energy absorption efficiency due to reinforced structures. Lin Sang et al. [70] proposed a novel crash box composed of an aluminum shell and a 3D-printed lattice core to achieve multi-objective optimization for the application. Wu et al. [71] developed a nacre-inspired cement-resin composite with a graded brick-mortar architecture, achieving superior flexural strength, toughness, and impact resistance. Daynes et al. [72] established a lattice structure analysis model to optimize the maximum energy absorption capacity of such systems. Despite these advances, experimental stress-strain curves for these structures typically exhibit only a single load-bearing plateau, limiting their effectiveness under multiple impacts of varying magnitudes.

The CorTube structure, a novel metamaterial configuration introduced by Zhang et al. [73] and Li et al. [74], integrates alternating corrugated plates and tubular elements to achieve enhanced energy absorption and impact resistance. By modulating the corrugation angle and tube diameter, the performance of the CorTube structure can be optimized, offering potential solutions to the aforementioned limitations. Nevertheless, the adaptability and recoverability of current designs under repeated compressive loading remain constrained.

Shape memory polymers (SMPs) and 4D printing technology have received extensive research attention this year. SMPs can achieve deformation memory and recovery under thermal, electrical, optical, and magnetic stimuli [71,72,75,76], and combined with 3D printing, they can achieve programmable manufacturing of complex structures [77–83]. 4D printing gives metamaterials adjustable mechanical properties and reusability [84–89]. This emerging technology brings new opportunities and challenges to the design of programmable and reusable energy-absorbing metamaterials. Recent studies have increasingly focused on the reusable mechanical behavior of energy-absorbing metamaterials based on shape memory polymers (SMPs). For example, Zhang et al. [90] studied the reusability and energy dissipation characteristics of 4D printed honeycomb metamaterials with different materials and structures through cyclic cold programming experiments. Dong et al. [91] used 4D printing technology to develop a reusable continuous fiber reinforced composite structure that exhibited excellent reusability, a shape recovery rate of >90%, and maintained strong energy absorption capacity after 6 test cycles. In addition, Zhang et al. [92] reported a multifunctional smart metamaterial inspired by biological load-bearing arc structures, which was fabricated using 4D printing technology. This innovative material exhibited programmable shape deformation, highly tunable mechanical properties, and reusability.

This study proposes a reconfigurable gradient mechanical metamaterial system that combines the CorTube gradient structure, shape memory polylactic acid (PLA) and 4D printing. The system offers several key innovations. Firstly, the Corrugated plate-tube (CorTube) gradient structure features adjustable parameters, including corrugation angle, tube diameter, and spatial gradient, which enable adaptation to non-uniform loads. In addition, by combining shape memory PLA with fused deposition modeling (FDM) 3D printing technology, the system achieves thermally activated structural recovery. Furthermore, even after fabrication, the mechanical properties of the structure can be reconfigured through high-temperature deformation, thereby overcoming the limitation of conventional metamaterials whose properties are fixed after manufacturing. Experimental and computational analysis show that the CorTube system exhibits a gradient-related stress-strain response under compression and can effectively adapt to spatially non-uniform load distribution. After being subjected to a 60% compressive strain, the structure can fully recover its initial structure within 5 s at a temperature of 80 °C and maintain stable energy absorption performance after the second loading (stress-strain curve deviation <3.2%). This integration of hierarchical design and active reconfiguration capabilities establishes a new framework for developing multi-cycle reusable, dynamically adaptive energy absorption systems.

This paper is organized into five sections. Section 2 outlines the conceptual design principles, geometric parameterization, and fabrication processes of the proposed CorTube gradient metamaterials using 4D printing technology. Section 3 details the comprehensive experimental methodologies and computational frameworks, including quasi-static compression testing, finite element modeling, and cyclic shape-recovery protocols. Section 4 presents an in-depth discussion of the results, elucidating the correlations between geometric gradients, multi-stage deformation mechanisms, and multi-cycle reusable energy-absorption performance. Finally, Section 5 draws the main conclusions, highlighting the advantages, structural boundaries, and potential engineering applications of the developed metamaterial system.

2. Design and fabrication

This section first presents three design concepts for CorTube metamaterials exhibiting gradient characteristics, followed by a detailed description of their fabrication processes. The CorTube structure consists of corrugated sheets and tubes, which have good energy absorption potential. The simple structural design simplifies the manufacturing process, and its mechanical properties can be strictly defined by 4 independent parameters. Crucially, energy absorption performance varies significantly with parameter adjustments. A dimension underexplored in prior studies that primarily examined horizontally compressed CorTube systems with uniform parameters [93]. Here, we systematically investigate the vertical compression response of CorTube variants featuring both parameter-tuned and gradient-enhanced designs.

2.1. Design of the CorTube structure

Each CorTube unit comprises vertically stacked corrugated plates and tubes, with in-plane key parameters defined in Fig. 1(a): corrugated plates are characterized by thickness (t), inclination angle (θ), and inter-tube horizontal spacing (L) where the horizontal distance of the tubes is expressed as the horizontal spacing between the centers of the two tubes, while tubular elements are defined by outer diameter (D) and wall thickness (t). All prototypes maintain constant plate and tube thicknesses (1 mm) and structural width (20 mm), length of crossbar (l = 4 mm) with detailed parameter combinations provided in Table A1. Fig. 1 (b)-(e) illustrates the three-dimensional configurations of the baseline CorTube unit and three gradient-optimized variants.

To facilitate experimental implementation and ensure the accuracy of the results, the CorTube structure designed in this study comprises four tubes in the first layer and three tubes in the subsequent layer. The horizontal positions of the centers of the three tubes in each subsequent layer are aligned with the midpoints of the lines connecting the centers of two adjacent tubes in the preceding layer. Following this arrangement, the CorTube structural unit consists of four layers, as illustrated in Fig. 1(b). Fig. 1(c)-(e) present three-dimensional models of CorTube structures with different gradient configurations. Specifically, Fig. 1(c) depicts a corrugated plate gradient structure, in which the corrugation angle θ increases incrementally from top to bottom, progressing from $\theta = 0°$ to $\theta = 15°$, and then decreasing back to $\theta = 0°$, with an angular increment of 5° per layer. The sequence of corrugation angles is 0-5-10-15-15-10-5-0. Fig. 1(d) shows a tube-spacing gradient structure, where the spacing L between tubes decreases from 35 mm to 27 mm and then increases back to 35 mm, with a step size of 4 mm per layer. The sequence of tube spacings is 35-31-27-27-31-35mm. Fig. 1(e) illustrates a tube diameter gradient structure, in which the tube diameter D increases from 4 mm to 6 mm and then decreases back to 4 mm, with a step size of 1 mm per layer. The sequence of tube diameters is 4-5-6-6-5-4 mm. Beyond this visual correspondence, Fig. S11 further clarifies the fundamental design rationale of the gradient architecture. The spatial arrangement of local geometric parameters (e.g., θ, L, D) across different layers directly dictates the sequential activation of collapse. By comparing the uniform unit in Fig. S11(a) and the graded assembly in Fig. S11(b), readers can intuitively grasp how a strategic variation of a single parameter along the vertical direction transforms a single-stage collapse into a multi-stage progressive mode. This figure thus serves as a critical link between the basic unit characterization (Section 4.2) and the gradient-driven performance enhancement (Section 4.3).

In addition to these three gradient configurations, to more comprehensively explore the potential impact of gradient change patterns (such as "decreasing-increasing", "increasing-decreasing", "decreasing-decreasing", etc.) on performance, two other gradient structures are

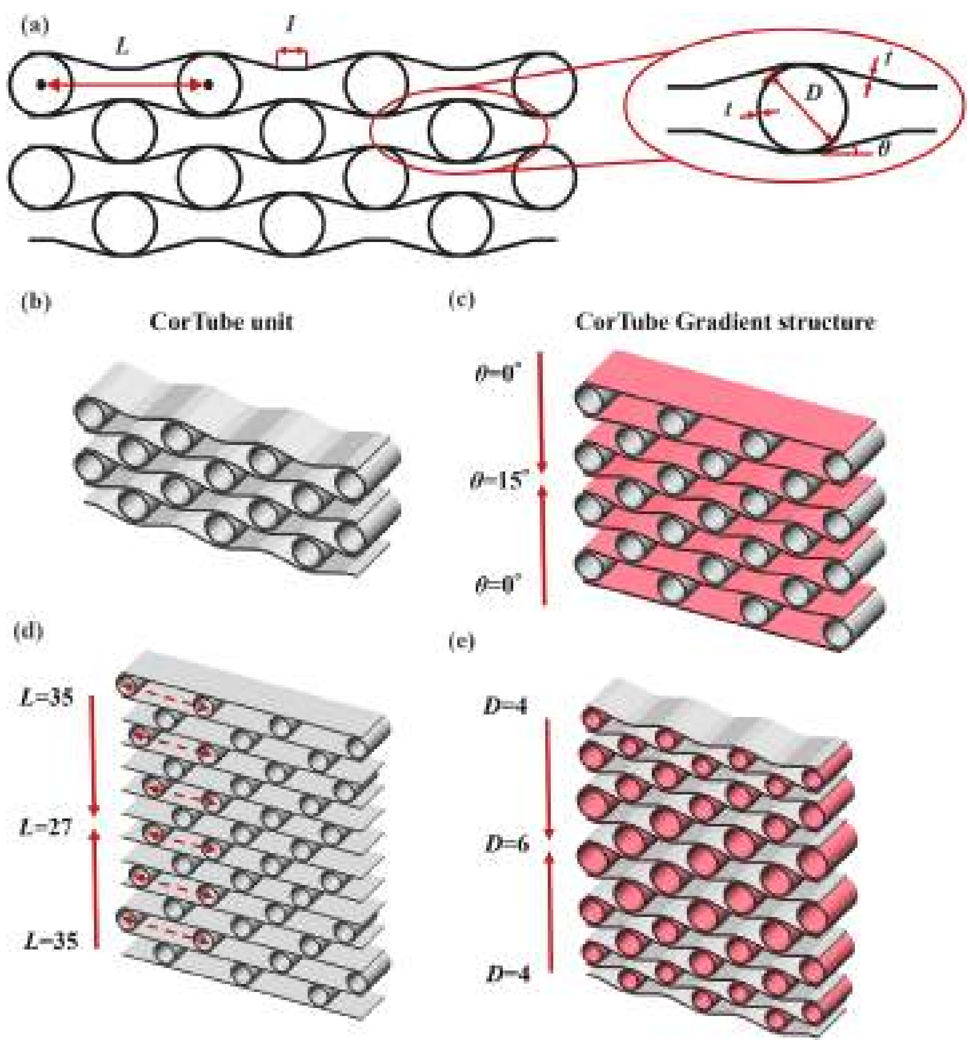

Fig. 1. CorTube Structural Design: (a) Sketch of the CorTube structural unit. Its main design parameters are the corrugation angle θ, the outer diameter of the tube D, and the spacing between the center points of the tube L (the structural thickness t designed in this study is fixed at 1 mm); (b) 3D model of CorTube structural unit, where the corrugated plate angle is 15° and the tube diameter is 5 mm; (c) 3D model of CorTube angle-gradient structure, where the corrugated plate angles are 0-5-10-15-15-10-5-0 (°) from top to bottom; (d) 3D model of CorTube tube-spacing gradient structure, where the tube spacings are 35-31-27-27-31-35 (mm) from top to bottom; (e) 3D model of CorTube tube size gradient structure, where the tube diameters are 4-5-6-6-5-4 (mm) from top to bottom.

derived for each gradient strategy by changing the gradient order. For instance, the corrugation angles in the additional two angle-gradient structures are arranged as 15-10-5-0-15-10-5-0 and 15-10-5-0-0-5-10-15 (see Supplementary Material Fig. S1-S10 for details). The design of these derived structures aims to systematically compare the effects of factors such as gradient direction, continuity, and the presence of a platform area. Table A1 summarizes the differences in parameter design among the various structures.

2.2. 4D printing of the CorTube structure

The design and modeling of the CorTube unit and gradient structure were performed in SolidWorks (version 2023). The CorTube units and gradient structures were fabricated via fused deposition modeling (FDM) 3D printing (Bambu A1 3D printer (Shenzhen Bambu Technology Co., Ltd. (Bambu Lab), Shenzhen, China)), leveraging its dimensional precision, cost efficiency, and high material utilization rates. Polylactic acid (PLA) was selected as the substrate material due to its balanced mechanical properties (Tensile modulus: 2800 MPa; the plastic properties of the material refer to our previous research [94]), shape memory capability, and compatibility with thermally activated structural reconfiguration. The shape-memory PLA filament used in this work was provided by the research group of Prof. Jinsong Leng (Harbin Institute of Technology) and has been extensively employed in previous studies on 4D printing and shape-memory structures, whose glass transition temperature (Tg) is 65 °C [95,96]. The key printing parameters were set as follows: nozzle temperature of 210 °C, build plate temperature of 60 °C, 100% cooling fan speed, printing speed of 150 mm/s, layer thickness of 0.2 mm, and wall thickness of 1 mm. All samples were printed with a unified orientation (printing layers horizontal, perpendicular to the compression loading direction). The minor FDM-induced anisotropy has a negligible effect on the mechanical performance due to the uniform infill, small layer thickness, and gradient structural design.

3. Quasi-static compression experiment of the CorTube structures

This section first introduces the purpose, method, and data processing method of the CorTube vertical compression experiment. Then, the method, parameters, and boundary conditions of the CorTube vertical compression simulation and structural shape memory behavior simulation are presented. Finally, the reusability cycle test method of energy absorption of room temperature compression-high temperature recovery is defined.

3.1. Experiments

The 4D printed CorTube unit and gradient structure were subjected to vertical compression, as shown in Fig. C1. Their load-strain responses were obtained, and the stress-strain curves were calculated to determine whether the design parameters, such as the corrugated plate angle θ, the tube spacing L, the tube diameter D, and the change of the gradient sequence had an impact on their mechanical behavior and characteristics. The deformation mode of the CorTube structure was studied to determine the relationship between the design parameter selection and the compression stress-strain.

Uniaxial compression tests were performed using a Zwick-010 universal testing machine with a loading speed of 5.0 mm/min. A mirrorless camera (EOS 5D Mark III, Canon) was used to record the compression process. Additionally, the compression modulus, energy absorption efficiency, densification strain, specific energy absorption (SEA), and plateau stress are defined as follows: [97,98]

$$E_y = \frac{\sigma_y}{\varepsilon_y} = \frac{F_y}{S_y} \Big/ \varepsilon_y, \tag{1}$$

where E_y denotes the compression modulus of the metamaterial, F_y is the compression load, S_y is the force-bearing area of the metamaterial, and ε_y represents the strain in the compression direction. The densification strain ε_d is defined as the engineering strain corresponding to the maximum energy absorption efficiency $\eta(\varepsilon)$, which can be written as follows:

$$\eta(\varepsilon_y) = \frac{\int_0^{\varepsilon_0} \sigma(\varepsilon_y) d\varepsilon}{\sigma(\varepsilon_0)}, \tag{2}$$

$$\left.\frac{d\eta(\varepsilon)}{d\varepsilon}\right|_{\varepsilon=\varepsilon_d} = 0, \tag{3}$$

where ε and $\sigma(\varepsilon_y)$ are the engineering strain and engineering stress, respectively. ε_0 represented the compressive strain obtained from experiments and simulations, and the corresponding compressive stress is $\sigma(\varepsilon_0)$. Due to the presence of multiple load plateaus in the stress-strain response, the corresponding energy absorption efficiency (EAE) curve may exhibit multiple local maxima. In the present study, the engineering stress-strain data were directly used to calculate the EAE curve according to Eq. (2), and the local maxima satisfying Eq. (3) were identified as the characteristic densification strains ε_{di} (i = 1, 2, 3) associated with different plateau stages. It should be noted that each local maximum of η(ε), denoted as ε_{di}, was regarded as the characteristic densification strain of the energy-absorption stage. It represents the strain at which the accumulated energy absorption, normalized by the instantaneous stress, reaches a local maximum. Therefore, ε_{di} was used as an indicator of the stage-wise absorption event, rather than as the exact boundary of the first plateau in the stress-strain curve. Since the experimental curves obtained under quasi-static compression were sufficiently smooth, no additional smoothing or filtering procedure was applied. The identification procedure is illustrated using a representative type2 gradient specimen in Fig. S12. The same procedure was applied consistently to all unit and gradient CorTube specimens to determine the energy absorption plateaus reported in Fig. 5.

After determining the densification strain, the plateau stress σ_{pj} (j = 1, 2, 3) is calculated by the following formula:

$$\sigma_{pj} = \frac{\int_{\varepsilon_{dj-1}}^{\varepsilon_{dj}} \sigma(\varepsilon) d\varepsilon}{\varepsilon_{dj} - \varepsilon_{dj-1}}, \tag{4}$$

The specific energy absorption (SEA) is calculated by:

$$SEA(\delta) = \frac{\int_0^{\delta_d} F(\delta) d\delta}{M}, \tag{5}$$

where M refers to the specimen's mass, and δ signifies the vertical compressive displacement, and $F(\delta)$ is the compression force at displacement δ. δ_d corresponds to the displacement at the densification strain. Then the energy absorbed per unit mass before densification was obtained and presented in Fig. 7.

To quantitatively evaluate shape recovery performance, the recovery rate (R_r) was defined as:

$$R_r = \frac{H_r - H_c}{H_0 - H_c} \times 100\%, \tag{6}$$

where H_0, H_c, and H_r denote the initial height, compressed height after unloading, and recovered height after thermal activation, respectively.

3.2. Finite element simulation of the compression process

As an effective supplement to experimental investigations, computational simulations provide unique benefits [99–101]. Specifically, finite element simulations facilitate detailed tracking of stress distribution, displacement, and thermodynamic behavior. In this research, numerical simulations were performed utilizing the finite element method

(FEM) within ABAQUS (version 2023) to assess the structural performance under vertical compression. The geometric representation was designed using SolidWorks (version 2023). The finite element model consists of both the CorTube structure and the compression platform, as depicted in Fig. C1. For meshing, 8-node reduced-integration hexahedral elements (C3D8R) were employed due to their capability to preserve computational accuracy, even in cases of mesh distortion [102, 103]. A mesh sensitivity analysis was conducted using global element sizes of 0.8 mm, 0.7 mm,0.6 mm, 0.5 mm, 0.45 mm, 0.4 mm, and 0.35 mm. The elastic modulus of the first linear phase was monitored as a convergence indicators. As shown in Fig. S13 and Table S1-S2, the differences between the 0.45 mm and 0.35 mm meshes were below 5%, indicating that further mesh refinement had a negligible influence on the predicted response. Therefore, a mesh size of 0.45 mm was selected in all simulations to balance accuracy and computational cost. "Hard" contact was specified for normal interactions, whereas a friction coefficient of 0.15 was assigned for tangential effects. The material's plastic characteristics were defined based on an ideal elastic-plastic model. Nominal stress-strain data were transformed into true stress-strain values before implementation in the simulation. The mechanical properties of PLA were incorporated using previously obtained experimental data (At 25 °C, the Young's modulus is 2800 MPa. For plastic properties, see references) [94], without considering material failure [104–106]. A displacement-controlled vertical load was applied at the reference point of the upper loading platform, while the lower platform was constrained. The force-displacement response of the finite element model was derived by tracking the reaction force and displacement at the reference point.

3.3. Finite element simulation of shape memory behavior

The deformation behavior of the CorTube structures was simulated by integrating the Williams-Landel-Ferry (WLF) time-temperature superposition principle with a generalized Maxwell model [107]. Model construction, compression loading, and meshing of the CorTube structure were performed as described in Section 3.2. To capture the material response at elevated temperatures, the Neo-Hookean model was implemented, while viscoelastic behavior was characterized using a Prony series in combination with the WLF equation. The relevant material parameters are summarized in Table B1. Stress relaxation data, obtained from our form research [94–96], were incorporated into the ABAQUS viscoelastic material module. Finite element simulations were conducted using Abaqus to investigate the shape memory effect of the 4D-printed CorTube structure under thermal stimulation. The simulations employed a coupled temperature–displacement solver, initializing the structure at 20 °C and applying a thermal load of 80 °C to emulate deformation in a hot water bath. The thermomechanical cycle comprised four distinct stages: high-temperature loading (0–100 s), cooling and fixation (100–200 s), unloading at low temperature (200–220 s), and high-temperature recovery (220–350 s). The shape programming process included the first three stages, while the final stage corresponded to shape recovery.

3.4. Multi-cycle reusability function verification

A cyclic compression-shape recovery test is carried out to evaluate the multi-cycle reusable energy absorption capacity of the 4D printed CorTube structures. (1) First, the CorTube structures were compressed to a strain of 0.7 at a constant speed of 5 mm/min at room temperature. (2) The load was maintained for 3 min to fix the shape of the structure (stress relaxation). (3) The specimen was unloaded at the same crosshead speed of 5 mm/min. (4) The specimen was heated in a water bath at 80 °C to restore its original shape and cooled, and subjected to the next test cycle. A total of six test cycles were performed to investigate the multi-cycle reusable energy absorption capacity of the CorTube structures.

4. Results and discussion

This section presents the compressive response, energy-absorption behavior, and reusable characteristics of the proposed 4D-printed CorTube metamaterial through a combined experimental, numerical, and mechanism-oriented analysis. It begins with the validation of the finite element model for capturing the early-stage response and dominant deformation sequence, and then examines how the key geometric parameters govern the local mechanical behavior of the unit structures. On this basis, the discussion is extended to gradient assemblies to reveal the experimentally observed progressive collapse and multi-stage plateau formation, which are subsequently interpreted using a mechanism-based theoretical framework. The section further evaluates the boundary of this mechanism under cyclic compression-thermal recovery conditions, and finally summarizes the energy-absorption map, design implications, and comparative performance of the CorTube system relative to representative energy-absorbing metamaterials.

4.1. Comparison between simulation and experiment

To establish a reliable basis for the subsequent mechanism analysis, the finite element model was first validated through compression experiments using the CorTube cell and representative gradient structures. As shown in Fig. 2, the simulated and experimental stress–strain curves exhibit good agreement in the early compression regime, particularly in terms of the initial slope and the first peak stress. Since the initial slope reflects the effective compressive stiffness of the structure, this agreement indicates that the present model can reasonably capture the geometry-dependent elastic response of the CorTube architecture. In particular, the simulation reproduced the phenomenon observed in the experiments where the stiffness increased as the tube spacing decreased. Moreover, the overall early responses of the gradient configurations remained close to each other because they contained the same constituent units, mainly the stacking sequence, rather than the differences in the unit composition.

Further validation is provided by the comparison of deformation snapshots between experiment and simulation, as shown in Fig. 3. The numerical model successfully reproduces the main sequence of structural evolution observed during uniaxial compression, including the initial bending of the corrugated plate, the progressive approach and contact of adjacent tubes, and the subsequent deformation of the outer and central tube regions. This consistency confirms that the model is capable of identifying the dominant deformation pathway in the early and intermediate stages of compression, which is essential for analyzing the activation sequence of different layers in the gradient structures. Therefore, the FE model is considered adequate for revealing the onset of local contact, the initial bending-dominated response, and the major progressive-collapse features of the CorTube design.

It should be noted, however, that deviations between simulation and experiment become more evident in the later deformation stage. This discrepancy mainly arises from two factors. First, geometric imperfections and fabrication inaccuracies introduced during the 3D-printing process are not fully represented in the idealized numerical model. Second, the constitutive description used in the compression simulation adopts an ideal elastic–plastic material model without accounting for material damage or crack formation, whereas local damage becomes increasingly important after large deformation. Therefore, the present numerical model is used in this work primarily as a tool for interpreting the early-stage stiffness, initial peak response, and deformation sequence, rather than for exact prediction of the damage-dominated post-collapse behavior. This validation scope is sufficient for the mechanism-oriented analysis developed in the following sections.

4.2. Geometry-dependent local response of CorTube structures

After validating the numerical model for the early-stage compression

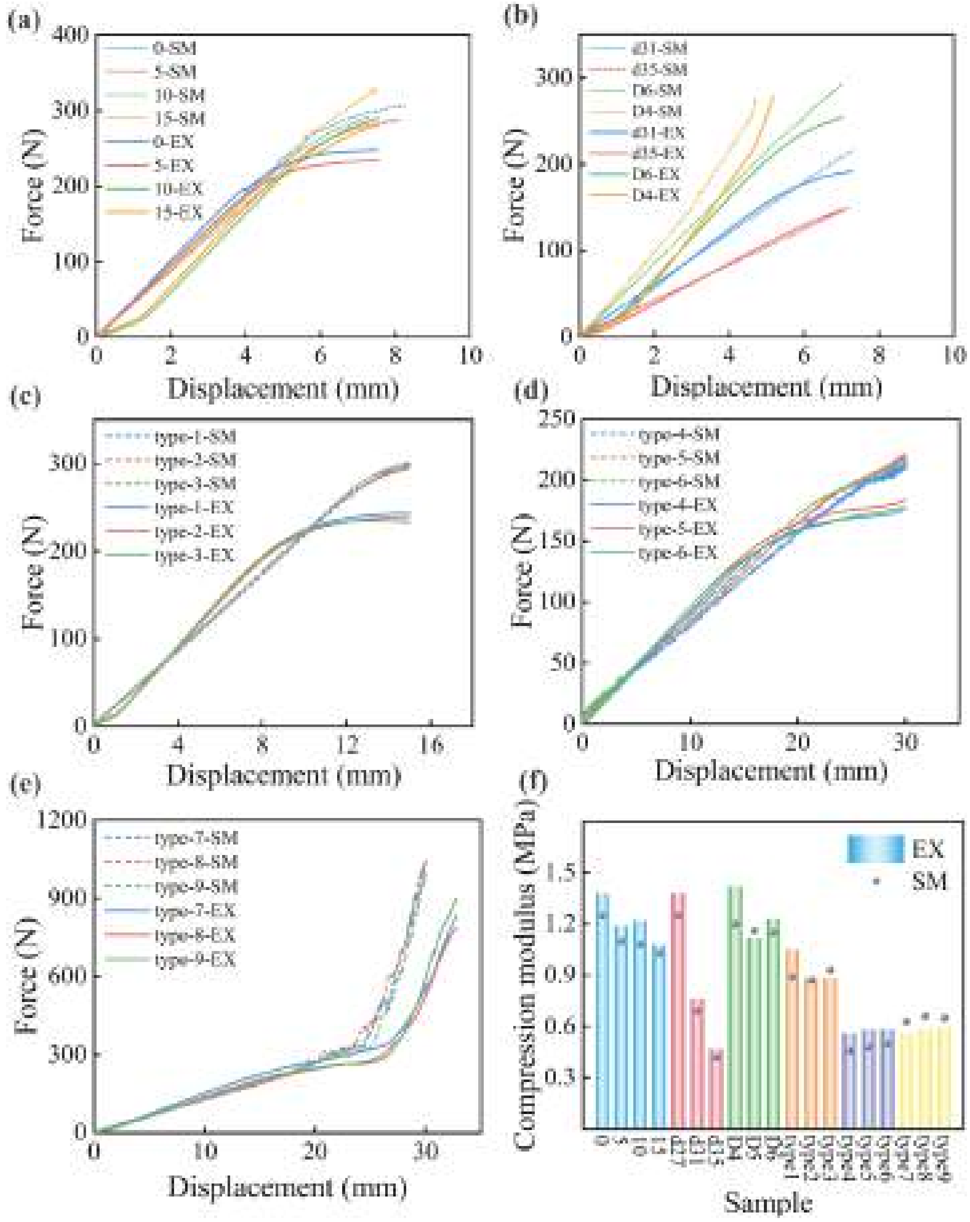

Fig. 2. Comparison of the consistency between compression tests and finite element simulations of different Cortube structures, where the dashed line represents the simulation results and the solid line represents the experimental results. The simulation and experimental results fit well in the linear stage, so the simulation can predict the compression modulus in the linear stage when the metamaterial is compressed. (a) Tube spacing element structures and Tube diameter element structures; (b) Corrugated plate angle element structures; (c) angle-gradient structures; (d) Tube spacing gradient structures; (e) Tube diameter gradient structures; (f) Compression modulus of the structures in the linear stage.

response, the first compression results are analyzed to identify how the key geometric parameters control the local deformation of the CorTube architecture. As shown in the Fig. D1, the CorTube unit exhibits a four-stage compression process, and the vertical compression results of the CorTube unit with different tube diameters and different tube spacings are shown in Supplementary Material Fig. S14 and S15. In Stage I, the stress–strain curve increases linearly. In Stage II, the curve approaches a plateau as the corrugated plates gradually bend and the slope decreases to nearly zero. Once adjacent corrugated plates come into contact, the dominant deformation mode shifts from corrugated-plate bending to tube compression, producing the subsequent rise and re-adjustment of the stress–strain response in Stage III. Finally, after progressive tube bending and deformation, the structure enters compaction and the stress–strain curve rises sharply in Stage IV. This evolution shows that the local response of the CorTube unit is governed by the competition between corrugated-plate bending, tube compression, and dense compression.

Quantitatively, the early-stage stiffness is highly sensitive to both tube diameter and tube spacing. In the diameter-controlled unit structures, reducing the tube diameter increases stiffness, and the $D = 4$ mm unit exhibits the highest stiffness of **1.42 MPa**. In the spacing-controlled unit structures, decreasing tube spacing causes a clear stiffness increase from **0.47 MPa** for **d35**, to **0.76 MPa** for **d31**, and to **1.38 MPa** for **d27** (Fig. 2(f)). These values indicate that tube spacing is the most direct parameter for controlling the structure compactness and the interaction between adjacent components, while tube diameter mainly affects the local curvature and bending resistance of the tubular elements. In contrast, the corrugated plate angle mainly affects the deformation compliance of the corrugated sheet itself and thus influences how the load is transferred before tube-dominated collapse begins.

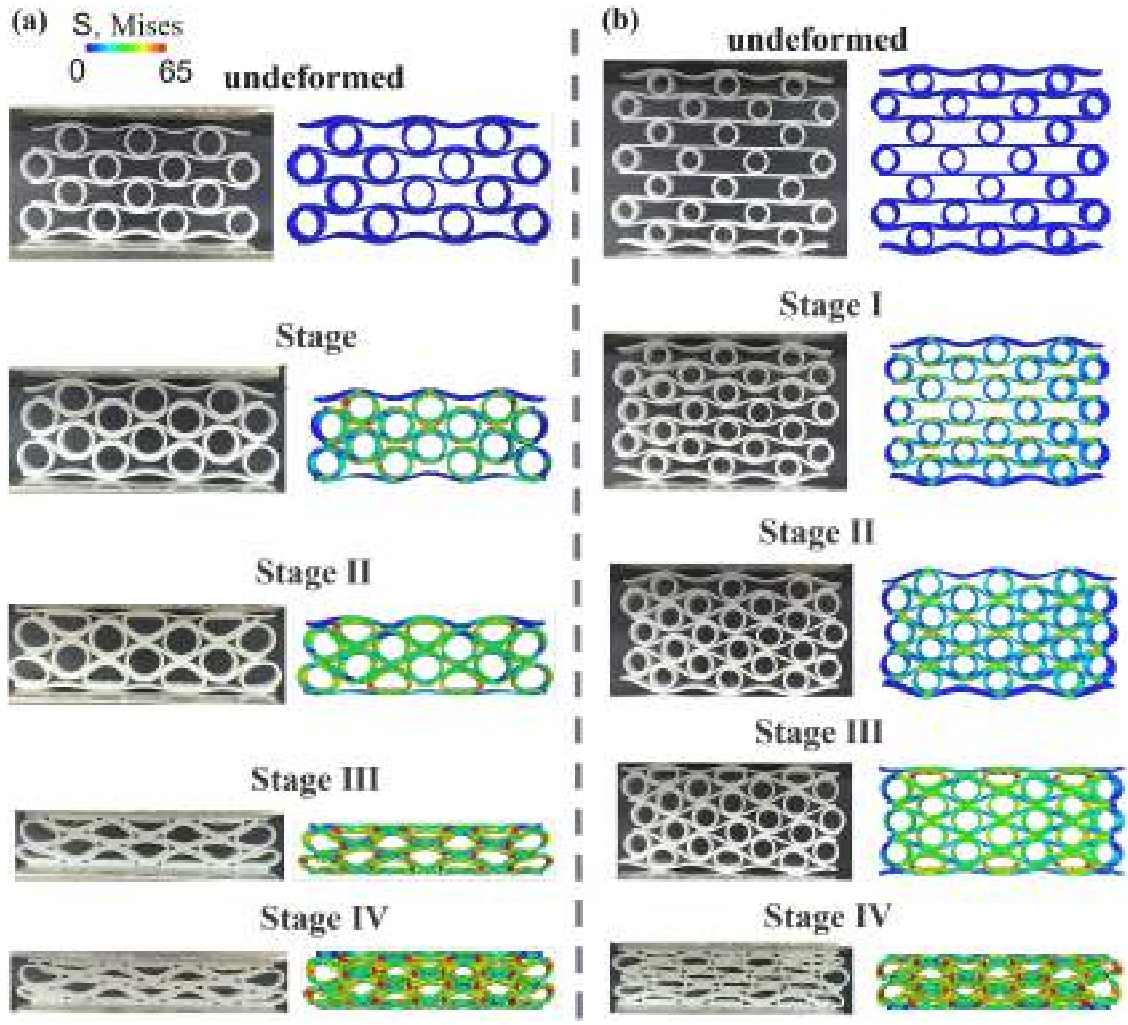

Fig. 3. Compressed image of the CorTube structure. The left side of each sub-image is the experimental result, and the right side represents the simulation result. (a) unit (D6); (b) angle-gradient structure (type3).

This parameter dependence is also reflected in the energy-absorption comparison of the unit structures. Fig. 5(a) shows that the specific energy absorption (SEA) of the unit structures increases as the corrugated plate angle decreases, and the unit with **0° corrugation angle** reaches the highest SEA of **0.136 J/g**. A similar trend is observed for tube spacing: the unit with the smallest spacing, **27 mm**, also reaches the maximum SEA of **0.136 J/g**. By contrast, the tube-size unit and the corresponding tube-size gradient structures show an indistinct plateau stage, indicating that diameter variation contributes less directly to plateau formation. Taken together, these results suggest that L primarily controls local contact closure and the initial load-bearing level, θ mainly regulates the local deformation path of the corrugated plate, and D mainly acts through local stability and curvature effects.

From the viewpoint of subsequent gradient design, these roles are mechanically distinct. The spacing parameter L provides the strongest control over the onset of local compaction; the corrugated angle θ has a significant influence on the deformation sequence when the structure deviates from the purely elastic state; and the diameter D mainly serves as a secondary correction to local tube stability. Therefore, the unit-level results establish the local mechanical basis for understanding why different gradient strategies later produce different degrees of plateau separation and energy-absorption enhancement.

4.3. Experimental evidence of progressive collapse in gradient CorTube structures

When the above geometric effects are spatially distributed along the loading direction, the compression response changes from the relatively concentrated collapse of a unit structure to a staged collapse of a gradient assembly. The three gradient structures considered in this article are the corrugated-angle gradient with the sequence, the tube-spacing gradient with the sequence, and the tube-diameter gradient with the sequence . Although these structures are assembled from the same constituent units, their compression curves exhibit markedly different stage divisions and plateau characteristics, demonstrating that the gradient sequence redistributes the activation sequence in different regions.

For the **angle-gradient structure** (Fig. 4a), the compression process can be divided into four stages. After the initial linear regime, the slope gradually decreases to zero before neighboring corrugated plates contact each other. The top and bottom tube layers are then compressed first, followed by the middle layer, producing a clearly staged response. Under vertical compression, the first stage extends to approximately **strain = 0.3~0.4**, which is a medium stage length among the tested configurations, but with a stronger initial energy-absorption effect and the **most obvious gradient effect**. Correspondingly, type1 angle-gradient structure can absorb non-uniform spatial loads of **1.5 MPa (I), 5 MPa (II), and 10 MPa (III)**, indicating a relatively wide multi-

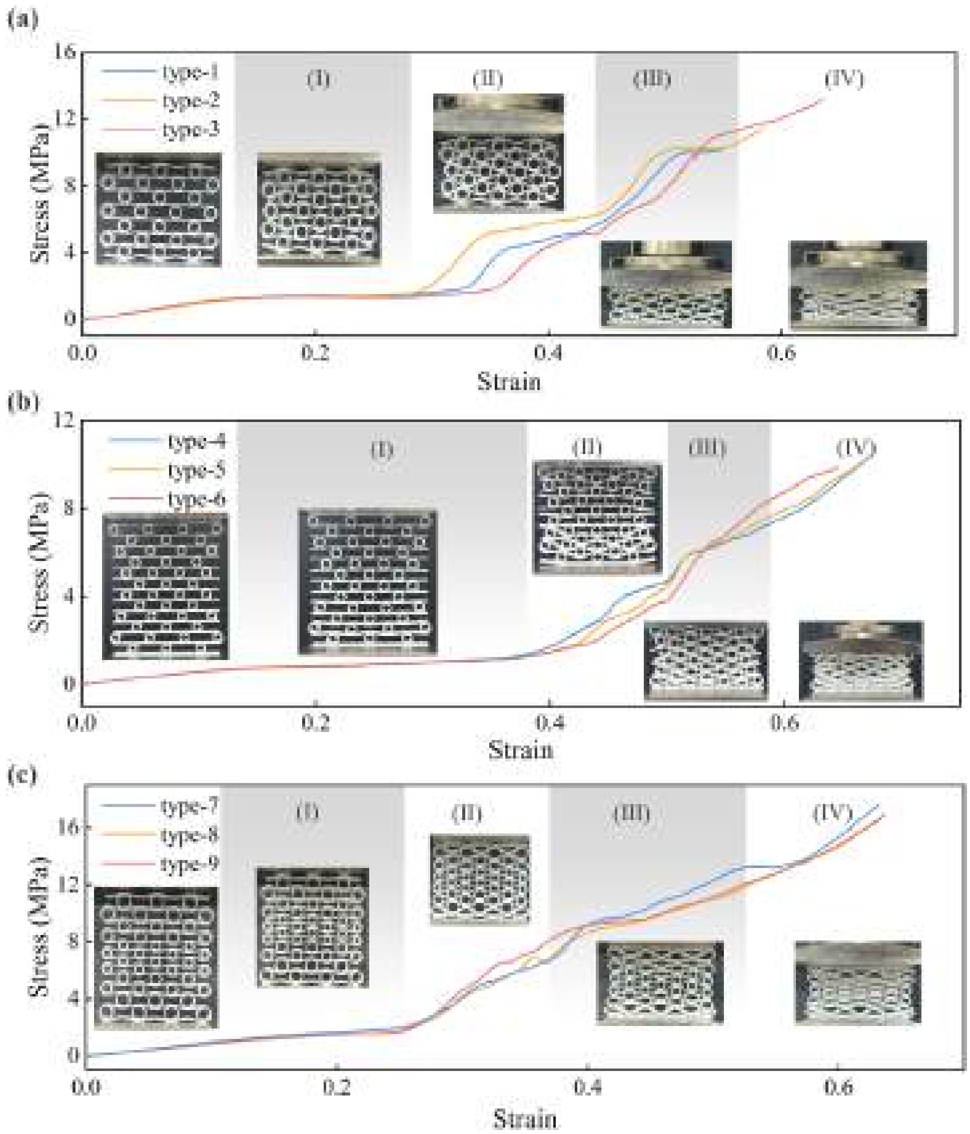

Fig. 4. Compression responses of three gradient CorTube structures: angle-gradient, tube-spacing gradient, and tube-diameter gradient. The stress-strain curve can be divided into 4 stages: (I) first load platform stage; (II) second compression stage; (III) third compression stage; (IV) densification stage. (a) CorTube angle-gradient structure experiment stress-strain curves (type1-type3), (b) CorTube tube-spacing gradient structure compression experiment compression experiment stress-strain curves (type4-type6); (c) CorTube tube size gradient structure compression experiment compression experiment stress-strain curves (type7-type9).

level load-bearing range.

For the **tube-spacing gradient structure**, the staged collapse is also clear, but its mechanical emphasis is different as shown in Fig. 4(b). The larger-spacing tubes first move closer and compact, after which the smaller-spacing tubes begin to approach and compact. Once corrugated plates contact each other, the uppermost and lowermost large-spacing tubes deform first, followed by the medium-spacing tubes and finally the smallest-spacing tubes. Under **strain = 0.4**, this structure exhibits the **longest first stage among all tested samples**, indicating the strongest initial energy-absorption capacity in the early compression range. In addition, type4 and type5 tube-spacing gradient structures still show a discernible gradient effect. Type4 structure can absorb non-uniform spatial loads of **1.0 MPa (I), 4.2 MPa (II), and 6.1 MPa (III).** However, the plateau regions in the second and third stages are relatively short, indicating energy absorption in the later-stage is relatively limited.

For the **tube-diameter gradient structure in** Fig. 4(c), the compression process progresses through four stages, but the distinction between the initial stages and the subsequent energy-absorption plateau is not well defined. The smaller tubes first move closer and compact, then the larger tubes begin to compress, followed by deformation of the medium-sized tubes and finally the smallest tubes. However, compared with the angle-gradient and tube-spacing gradient cases, the stress–-strain curves do not show a strongly separated plateau structure, except for the type7 tube-diameter gradient structure. This observation result is consistent with the subsequent quantitative comparison, indicating that the influence of tube size on the platform load size can be disregarded.

The quantitative comparison in Fig. 5(a) further clarifies the difference between gradient type and gradient arrangement. For the **first load plateau**, the SEA of the angle-gradient structures changes significantly with arrangement type: **type3 = 0.146 J/g, type1 = 0.127 J/g**, and **type2 = 0.082 J/g.** By contrast, the first-plateau SEA of the tube-spacing gradient structures remains relatively stable at about **0.12 J/g.** Fig. 5(a) (Red pillar) further shows that the **first load plateau is primarily affected by tube spacing**, whereas the corrugated plate angle has a comparatively smaller influence, and tube size has negligible influence on platform load magnitude. These results indicate that tube-spacing gradient mainly controls the onset position and stability of the

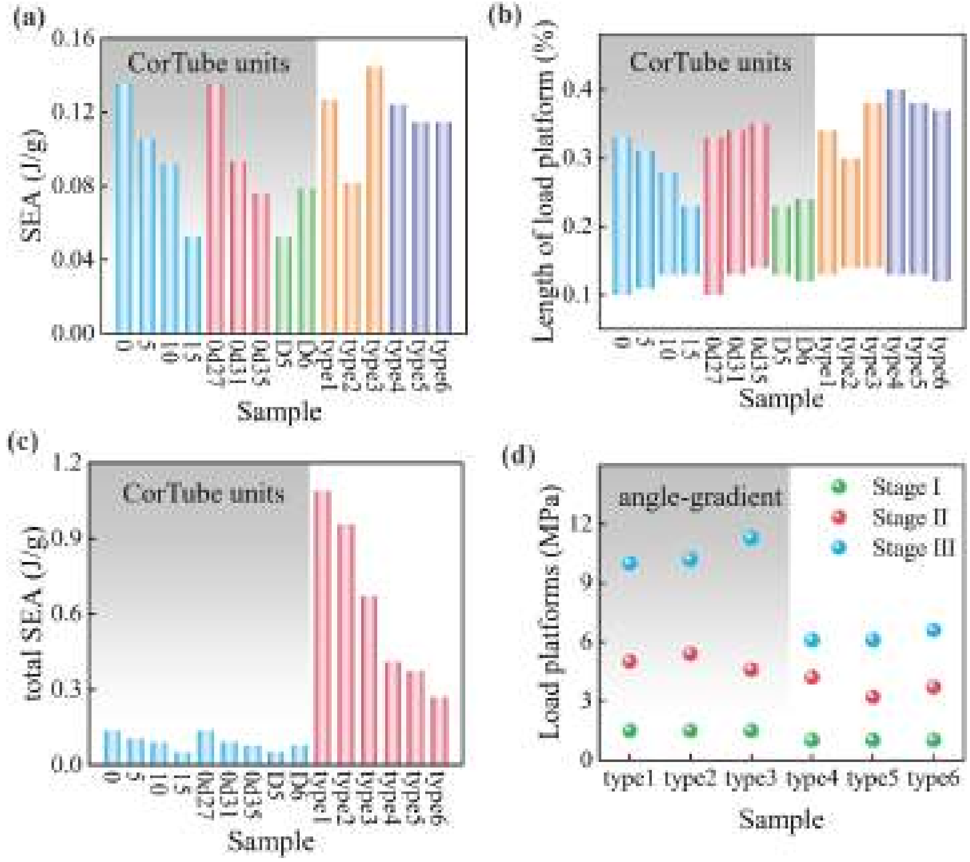

Fig. 5. Energy Absorption Performance Characterization of Cortube structures, (a) the first load plateau (Stage I) specific energy absorption; (b) Strain length of the first platform (Stage I); (c) The total specific energy absorption; (d) Different load platforms of Cortube gradient structures.

first plateau, while the angle gradient has a more significant regulatory effect on the sequence of collapses and the distribution of energy absorption over multiple periods.

This sequence effect becomes even clearer when the total energy absorption across all platform stages is considered. For the angle-gradient structures (Fig. 5c), the total SEA reaches **1.088 J/g** for **type1, 0.957 J/g** for **type2**, and **0.672 J/g** for **type3**. Compared with the best-performing homogeneous CorTube unit structure (SEA = 0.136 J/g), the angle-gradient assemblies achieved approximately 8.0-fold, 7.0-fold, and 4.9-fold increases in total SEA, respectively. Since SEA is normalized by specimen mass, these improvements reflect the effectiveness of the gradient-design strategy rather than an increase in structural mass. Moreover, the type1 angle-gradient structure exhibits **two additional load platforms** at **4.76 MPa** and **10.72 MPa** beyond the first platform shown in Fig. 5(d), which means that it can absorb compressive loads over a much wider range than the homogeneous unit structures. Therefore, the experimental comparison among the different gradient types and arrangement types directly supports the interpretation that the main function of gradient design is not merely to raise average stiffness, but to separate local activation events in space, thereby transforming single-stage collapse into tunable multi-stage progressive collapse.

4.4. Deformation mechanism interpretation and gradient design rules

To further clarify the relationship between geometric gradients and multi-stage load-plateau formation, a mechanism-guided analytical model is introduced in this section. The purpose of this model is not to exactly reproduce the full nonlinear stress-strain curve, because the compression of the CorTube structure involves large deformation, contact, local instability, plasticity, and damage accumulation. Instead, the model aims to identify how the geometric parameters redistribute the activation thresholds of different layers and thereby transform a concentrated collapse into a progressive layer-by-layer collapse.

At the structural scale, the effective mechanical response of the CorTube metamaterial is first influenced by its architecture-dependent relative density. For the present geometry, the relative density can be expressed in a simplified form as

$$\overline{\rho} = \frac{\rho^*}{\rho_s} = f(t/D, t/L, \theta), \tag{7}$$

where ρ^* and ρ_s are the densities of the metamaterial and the base material, respectively, t is the wall thickness, D is the tube diameter, L is the tube spacing, and θ is the corrugated plate angle. For bending-dominated cellular structures, the effective modulus and plateau stress generally follow the scaling trends

$$\frac{E^*}{E_s} \propto \overline{\rho}^n, \tag{8}$$

$$\frac{\sigma_{pl}}{\sigma_s} \propto \overline{\rho}^m, \tag{9}$$

where E^* and E_s are the effective modulus of the metamaterial and the modulus of the solid material, respectively, σ_{pl} is the plateau stress, σ_s is the characteristic strength of the base material, and n and m are scaling exponents associated with the dominant deformation mode. These relations explain why changing the tube spacing, corrugation angle, or tube diameter can modify the overall stiffness and load-bearing level of the CorTube structure. However, the emergence of multiple separated load plateaus cannot be explained by relative density alone. The key mechanism of the gradient CorTube structure is the separation of local activation events along the loading direction.

To describe this effect, a layer-dependent critical displacement $u_{c,i}$ is introduced for the i th layer. It is defined as the earliest displacement at which the layer begins to contribute significantly to stage-wise load bearing. This activation may be triggered by local contact, local bending/buckling instability, or local densification. Therefore,

$$u_{c,i} = \min\left(u_i^{con}, u_i^{buc}, u_i^{den}\right), \tag{10}$$

where u_i^{con}, u_i^{buc}, and u_i^{den} are the characteristic displacements associated with contact initiation, instability initiation, and local densification, respectively.

The contact-related contribution is mainly governed by the initial closable gap between neighboring structural members. For the CorTube architecture, this gap is affected primarily by the tube spacing L_i and the corrugated plate angle θ_i. In a first-order trend form,

$$u_i^{con} \sim \alpha_L(L_i - L_0) + \alpha_\theta h_i(1 - cos\theta_i), \tag{11}$$

where L_0 is a reference compact spacing, h_i is the effective corrugation height, and α_L and α_θ are geometric coefficients. This expression indicates that increasing the tube spacing or increasing the corrugation angle tends to delay the onset of effective contact.

The instability-related contribution is associated with the ratio between the local critical load and the equivalent stiffness of the layer,

$$u_i^{buc} \sim \frac{F_i^{cr}}{k_i}, \tag{12}$$

where F_i^{cr} is the local critical load and k_i is the equivalent stiffness of the i th layer. Since the early compression response of the CorTube structure is dominated by bending of the corrugated plates, the equivalent stiffness can be approximately expressed as

$$k_i \propto E_s t^3 L_i^{-3} \cos^p\theta_i, \tag{13}$$

where p is a geometric exponent related to the bending configuration. The local critical load is further affected by tube geometry, especially the tube diameter D_i, because the tube diameter modifies local curvature, bending resistance, and tube stability. Therefore, D_i acts mainly as a correction factor for the instability threshold rather than as the dominant parameter controlling plateau separation.

The densification-related contribution is related to the remaining compressible geometric space before local compaction becomes dominant. It can be written in a trend form as

$$u_i^{den} \sim \gamma_L L_i + \gamma_\theta h_i sin\theta_i - \gamma_D D_i, \tag{14}$$

where γ_L, γ_θ, and γ_D are geometric coefficients. This relation indicates that larger tube spacing and larger corrugation deformation capacity tend to postpone densification, whereas a larger tube diameter reduces the available compaction space and may promote earlier local densification.

Combining these three contributions, the layer-dependent critical displacement can be expressed as

$$u_{c,i} = \min\left[\alpha_L(L_i - L_0) + \alpha_\theta h_i(1 - cos\theta_i), \frac{F_i^{cr}}{k_i}, \gamma_L L_i + \gamma_\theta h_i sin\theta_i - \gamma_D D_i\right]. \tag{15}$$

This expression provides a simplified analytical basis for understanding the role of the three gradient parameters. The tube spacing L_i directly changes the contact-closure distance and the local densification displacement, and therefore strongly affects the onset and stability of the first load plateau. The corrugated plate angle θ_i mainly changes the bending compliance of the corrugated plates and the load-transfer path, thus controlling the collapse sequence and the separation between successive plateaus. The tube diameter D_i mainly modifies local tube curvature and stability, and therefore serves as a secondary tuning parameter for local response refinement.

For a homogeneous CorTube structure, the geometric parameters of different layers are identical or very close, so the corresponding critical displacements are also close. In this case, several layers tend to be activated almost simultaneously once the critical condition is reached, resulting in a relatively concentrated collapse and a single dominant plateau. In contrast, for a gradient CorTube structure, the geometric parameters are intentionally distributed along the loading direction. If the layer-wise critical displacements satisfy

$$u_{c,1} < u_{c,2} < \cdots < u_{c,n}, \tag{16}$$

the local collapse events are spatially and temporally separated. The first activated layer enters local collapse and absorbs energy, while the remaining layers still stay in the pre-collapse or elastic stage. With increasing compression displacement, subsequent layers are activated one after another. As a result, the global compression response becomes the superposition of multiple local collapse processes rather than a single collective instability event.

Accordingly, the global compressive force can be approximately described as

$$F(u) \approx \sum_{i=1}^{n} H(u - u_{c,i}) F_{p,i}. \tag{17}$$

where $H()$ is the Heaviside function and $F_{p,i}$ is the average plateau contribution of the i th layer after activation. This formulation explains the formation of multi-stage load plateaus: each newly activated layer contributes an additional load-bearing component, while the spacing between adjacent $u_{c,i}$ values determines the position, width, and separation of the plateau stages. When the differences between neighboring critical displacements are sufficiently large, distinct multi-stage plateaus can be formed. When several $u_{c,i}$ values are close to each other, neighboring layers collapse nearly simultaneously, and the plateau stages become merged or less distinguishable.

The three gradient strategies modify $u_{c,i}$ through different physical pathways. For the tube-spacing gradient, defined in Section 2.1 as the sequence inter-tube horizontal spacing L, the primary effect is the variation of local closure distance between neighboring members. A larger local spacing increases the displacement required before adjacent members come into effective contact, whereas a smaller spacing promotes earlier interaction and earlier compaction. Therefore, the spacing gradient mainly separates u_i^{con} and u_i^{den} between neighboring layers. This interpretation agrees with the quantitative comparison in Fig. 5(b) and Supplementary material Fig. S15, which shows that the first load plateau load is primarily affected by tube spacing, while the first-plateau SEA of the tube-spacing gradient structures remains relatively stable at approximately 0.12 J/g. The corresponding deformation images in the tube-spacing gradient compression tests further show that different tube-spacing regions are activated successively, producing a relatively clear staged response.

For the corrugated-angle gradient, defined as CorTube angle-gradient structures, the main effect is not a strong change in the first plateau load, but a redistribution of the deformation path and collapse order through the bending compliance of the corrugated plates. In the present framework, this effect is mainly reflected in u_i^{buc}, because the local onset of tube-dominated collapse depends on how each corrugated layer bends, rotates, and transfers compressive load to adjacent tubes. This explains why Fig. 5(a) shows a pronounced dependence of the first-plateau (Stage I) SEA on gradient arrangement for the angle-gradient structures, with values of 0.146 J/g, 0.127 J/g, and 0.082 J/g for types3, 1, and 2, respectively, and why the total SEA across all platform stages in Fig. 5(c) differs even more strongly, reaching 1.088 J/g for type1, 0.957 J/g for type2, and 0.672 J/g for type3. Therefore, the angle gradient mainly controls the spacing between successive activation events rather than the magnitude of the initial itself.

For the tube-diameter gradient, the effect on $u_{c,i}$ is more indirect.

Changing tube diameter modifies local curvature, local bending resistance, and local tube stability, but it does not separate the contact-closure condition as directly as tube spacing, nor does it re-route the deformation path as strongly as corrugation angle. As a result, its influence acts mainly as a correction to the local threshold distribution rather than as the dominant source of plateau separation. This interpretation is consistent with the observation in Supplementary material Fig. S17 that tube size *D* has a negligible influence on the platform load magnitude, as well as with the weaker stage separation observed in the tube-diameter-gradient compression response.

Based on this mechanism, the gradient design rules of the CorTube metamaterial can be summarized as follows. The tube-spacing gradient is the most direct parameter for regulating the onset position of the first plateau and delaying local densification. The corrugation-angle gradient is the key parameter for tuning the collapse sequence, plateau width, and multi-stage load regulation. The tube-diameter gradient is more suitable as a secondary parameter for refining local stability rather than as the primary route for generating separated plateaus. Therefore, the design target of the gradient CorTube structure is not to maximize a single geometric gradient, but to construct an ordered distribution of layer-wise critical displacements, thereby achieving progressive collapse, broadened load plateaus, and enhanced energy absorption.

4.5. Reusability and damage-induced degradation of stage-wise collapse

To further assess the practical significance of the mechanism established in Sections 4.3 and 4.4, cyclic compression–thermal recovery tests were performed to determine whether the stage-wise collapse behavior can be repeatedly retained after shape recovery. The shape-memory behavior of the employed PLA material has been systematically characterized in previous studies [95,96]. The recovery process used in the present work relies on thermally activated molecular-chain mobility above the glass-transition temperature, enabling rapid recovery of the programmed structure. According to the test protocol described in Section 3.4, the CorTube structures were compressed at room temperature, unloaded, thermally recovered in an 80 °C water bath, and then subjected to the next loading cycle, for a total of six cycles. The recovery rate was calculated according to Eq. (6). As shown in Fig. E1 and Supplementary Video, all compressed structures were able to recover their original shapes after heating. For the representative gradient configurations type2 and type5, compressed to 60% and 55% strain, respectively, full shape recovery was achieved within 5 s, with a recovery rate of 99%, shown in Fig. E1 and Fig. 6(a) and (b). Fig. S22 shows the thermo-mechanical cycle process simulation of CorTube structures. The recovery-rate curves in Fig. 6(c) and (d) further show that both structures maintained recovery rates above 90% during the first three thermo-mechanical cycles. These results indicate that the geometric configuration responsible for the initial activation sequence can be largely restored after thermal recovery, providing the structural basis for repeatable staged compression behavior.

The repeated compression results shown in Fig. 7 reveal that the stage-wise collapse mechanism is not lost immediately after cycling, but instead degrades selectively with increasing cycle number. In particular, the stress-strain curves of the first and second compressions show a high degree of consistency, and for all tested structures, the linear region and the first load plateau remain almost unchanged throughout the six compression cycles. By contrast, the second and third plateau stages begin to show noticeable differences during the first three cycles and deteriorate more clearly from the fourth cycle onward. As the number of cycles increases, the slope in the third-plateau region rises progressively, indicating that the plateau gradually disappears and that the corresponding energy-absorption stage weakens. This trend demonstrates that the early-stage activation threshold remains comparatively robust under repeated recovery, whereas the later stage-wise collapse

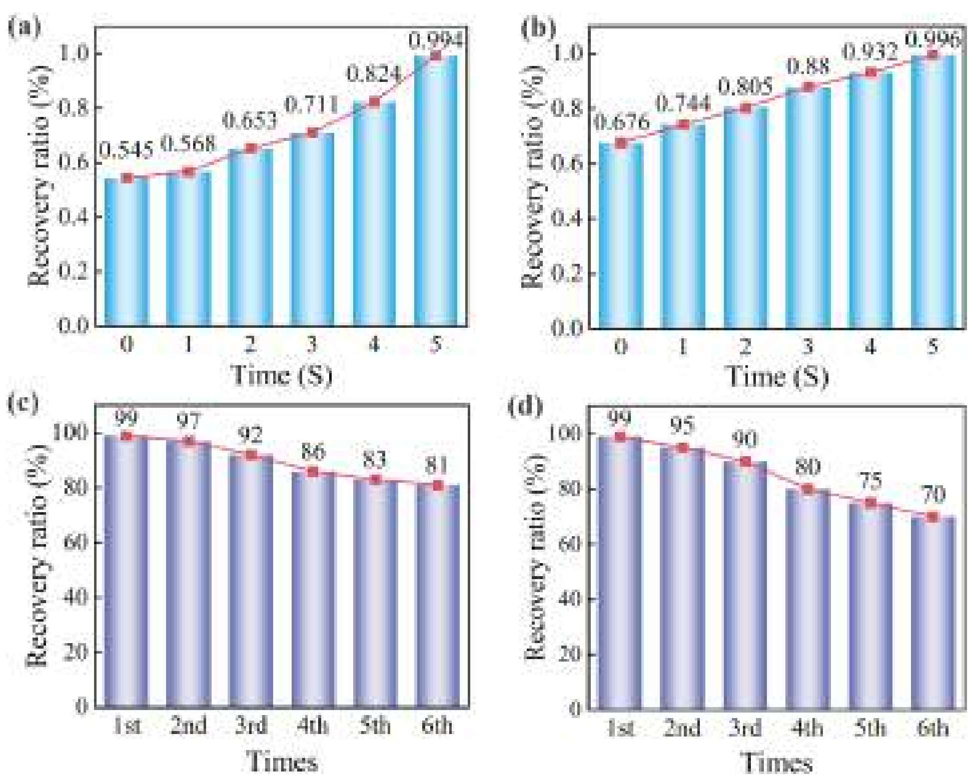

Fig. 6. Relationship between shape recovery rate, thermal stimulation time and cycle times of CorTube gradient structures: (a) The relationship between the shape recovery rate of the type2 gradient structure and the thermal stimulation time; (b) The relationship between the shape recovery rate of the type5 gradient structure and the thermal stimulation time; (c) The relationship between the shape recovery rate of the type2 gradient structure and the number of compressions; (d) The relationship between the shape recovery rate of the type5 gradient structure and the number of compressions.

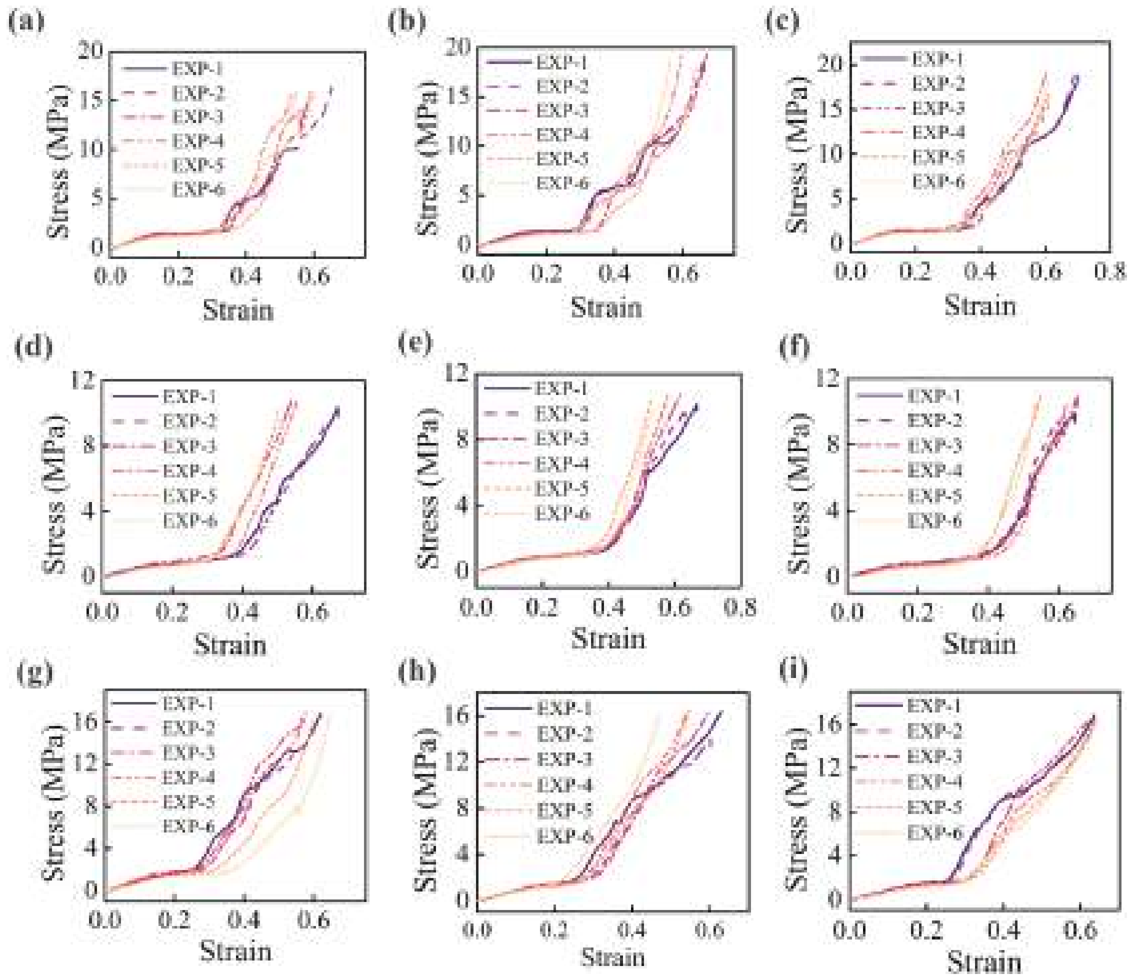

Fig. 7. Comparison of stress-strain curves for the CorTube gradient structure metamaterials during six cycles of compression. The solid line represents the result of the first compression test, while the dashed lines correspond to the curves after each subsequent recovery. The density and lightness of the dashed lines indicate the number of cycles: the denser and lighter the dashed line, the greater the number of cycles. (a) type1; (b) type2; (c) type3; (d) type4; (e) type5; (f) type6; (g) type7; (h) type8; (i) type9.

mechanism is more vulnerable to accumulated structural damage.

This selective degradation can be understood as a boundary condition of the $u_{c,i}$-based framework proposed in Section 4.4. The first load plateau mainly corresponds to the earliest activation events, which are governed primarily by recoverable geometric closure and bending-dominated response of relatively less damaged regions. In contrast, the later plateaus depend on deeper local tube deformation and repeated load transfer through regions that experience larger strain concentration during compression. Once these tube regions accumulate damage, the corresponding layer-wise critical displacements $u_{c,i}$ are no longer cleanly separated, and the originally distinct local activation events become increasingly merged. As a result, the second and third plateau stages lose their clear stress-separation characteristics even though the overall structure can still recover its external shape. Therefore, thermal shape recovery restores the macroscopic geometry, but cannot fully erase the accumulated local damage that controls the later-stage collapse sequence. This interpretation is consistent with the crack formation observed after the third compression cycle, where some tubes developed cracks along the horizontal diameter and the tube structure became weakened.

The quantitative comparison in Fig. 7(a–c) further supports this interpretation. For the corrugated-angle-gradient type2 structure, the linear region and the first load plateau of all six cycles show obvious overlap, whereas the second and third load plateaus begin to disappear in the fourth cycle. At that stage, the stresses of the second and third plateaus are 4.77 MPa and 10.49 MPa, respectively, corresponding to 88.3% and 92.8% of their initial values. Combined with the comparison between the first and sixth compression results summarized in Fig. F1 (a)-(b), these results indicate that the CorTube structure not only remain its recoverable shape after recovery, but also retains a substantial portion of its early-stage load-bearing ability (compression process in Supplementary Material Fig. S16-S21). However, the gradual degradation of the later plateaus also defines the mechanism boundary of the present design. The reusability is strong for the initial stage-wise response, while the deeper multi-stage collapse behavior is progressively limited by damage accumulation in the tube regions.

To further assess the practical limit of cyclic reusability, an additional seventh thermo-mechanical cycle was conducted for the representative type3 structure. As shown in Fig. S23, a pronounced degradation of the stress-strain response and energy-absorption capability was observed after the seventh cycle. This result indicates that damage accumulation becomes dominant after repeated loading and recovery, leading to a substantial loss of the multi-stage energy-absorption functionality. Therefore, the present PLA-based CorTube metamaterials should be regarded as limited-cycle reusable structures rather than indefinitely reusable systems.

Notably, the tube-spacing gradient structure (type5) exhibits a more severe degradation in recovery rate (≈78% after six cycles) than the angle-gradient structure (type2, ≈90%). This difference stems from the distinct stress distribution characteristics of the two gradient designs.

The symmetric tube-spacing gradient (35–31–27–27–31–35) induces significant local stress concentration at the interlayer spacing transition regions during cyclic loading. Repeated compression-recovery cycles intensify local extrusion and shear stress at these joints, and the inherent brittleness of shape-memory PLA promotes microcrack initiation and propagation, accelerating damage accumulation. In contrast, the angle-gradient structure undergoes more uniform deformation with evenly distributed stress, minimizing local stress concentration and micro-damage accumulation, thus maintaining a higher recovery rate.

From an application perspective, these observations suggest that the multi-cycle reusable advantage of the CorTube system lies in maintaining and repeatability of the initial platform and the early progressive-collapse response, which is critical for the buffering and load regulation functions in the first stage. By contrast, the later-stage plateaus should be regarded as more damage-sensitive energy-absorption reserves. Therefore, the present CorTube design combines thermal recoverability with partial mechanical reusability, while also revealing a clear trade-off between repeated shape restoration and the long-term retention of fully separated stage-wise collapse.

4.6. Energy absorption map and design implications

The results presented in Sections 4.2–4.5 indicate that the energy-absorption behavior of the CorTube system should not be evaluated solely by a single SEA value, but rather by a combined map of load level, plateau distribution, total energy absorption, and recoverability. In this sense, the gradient CorTube structures outperform the unit structures in two complementary ways. First, they broaden the accessible load-bearing range by generating multiple stress plateaus instead of a single dominant plateau. Second, they enhance the cumulative energy absorption over the whole compression process. As shown in Fig. 5(c), the total SEA of the corrugated-angle-gradient structures reaches 1.088 J/g, 0.957 J/g, and 0.672 J/g for type1, type2, and type3, respectively. Compared with the best-performing unit structure (0.136 J/g), these values correspond to improvements of 8.0-fold, 7.0-fold, and 4.9-fold. Moreover, the type1 angle-gradient structure exhibits two additional load platforms at 4.76 MPa and 10.72 MPa beyond the first platform (Fig. 5(d)). The result demonstrates that gradient design increases not only the absorbed energy, but also the range of loads that can be effectively managed by a single structure.

A further design implication is that different gradient parameters are suitable for different performance objectives. The comparison in Fig. 5 (a)-(b) shows that the first load plateau is mainly affected by tube distance, while the influence of the corrugated plate angle is relatively small. The influence of the tube size on the platform load magnitude can be disregarded. Correspondingly, the first-plateau SEA of the tube-spacing-gradient structures remains relatively stable at approximately 0.12 J/g. The angle-gradient structures are much more sensitive to arrangement sequence, with first-plateau SEA values of 0.146 J/g, 0.127 J/g, and 0.082 J/g for type3, type1, and type2, respectively. These results suggest a practical design map for the CorTube system. When the main objective is to stabilize the initial plateau level and provide early-stage buffering, the tube-spacing gradient is the preferred strategy. When the goal is to regulate the number, separation, and distribution of multiple plateaus across a broader load range corrugation-angle gradient is more effective. The tube-diameter gradient is more suitable as a secondary tuning parameter for local response refinement rather than as the principal route for generating clear plateau separation.

The engineering value of this design map is reinforced by the combination of lightweight construction and partial mechanical reusability. As noted in Section 4.5, the CorTube structures can recover their original shape within 5 s after thermal activation, while retaining a highly stable initial plateau response over repeated cycles; at the same time, the densest configuration in the present study still has a low density of only 0.347 g/cm^3 (Supplementary Material Table S3). Therefore, the proposed CorTube system is particularly attractive for applications requiring lightweight, multi-cycle reusable, and load-adaptive buffering. In practical terms, the early plateau can be exploited as a repeatable first-stage buffer, while the later plateaus may serve as damage-sensitive reserve absorption stages. Thus, the main design target of the CorTube metamaterial is not simply to maximize a single geometric gradient or a single SEA value, but to achieve an ordered combination of plateau position, plateau number, load range, total energy absorption, and recoverable service response. From this perspective, the CorTube system provides a viable design framework for reusable buffering components, personal protective structures, and other mechanically adaptive energy-absorbing devices.

4.7. Performance comparison with representative energy-absorbing metamaterials

To further position the proposed CorTube system within the broader family of energy-absorbing metamaterials, a comparative benchmark was established using representative corrugated, honeycomb, auxetic, graded, and 4D-printed recoverable structures [108–114], as summarized in Fig. 8. Since the compared studies involve different material systems, densities, loading conditions, and evaluation metrics, this work does not intend to conduct a strict one-to-one ranking based on a single index. Instead, it is used to compare the functional capabilities of different structures in terms of energy-absorption-related enhancement, plateau characteristics, and recoverability. Under this perspective, many reported designs mainly focus on improving the ability of specific energy absorption or crushing efficiency, whereas relatively few simultaneously provide gradient-programmed multi-stage load regulation, broad load-range adaptability, and reusable service response.

From the viewpoint of relative enhancement (Fig. 8a), the CorTube gradient structures show competitive performance compared with several representative absorbers. The present angle-gradient CorTube reaches total SEA values of 1.088 J/g, 0.957 J/g, and 0.672 J/g for type1, type2, and type3, corresponding to increases of 8.0-fold, 7.0-fold, and 4.9-fold, respectively, relative to the best-performing unit structure. By comparison, the crossed star-shaped honeycomb [108] reports a 244.98% increase in SEA, the machine-learning-optimized graded honeycomb [110] improves energy absorption by 66% and 40% for hexagonal and auxetic configurations, the multi-material re-entrant [111] and hexagonal lattices enhance SEA by 60% and 15%, and the corrugated gradient auxetic structure [109] increases SEA by up to 81.5% under the reported geometric condition. In addition, several advanced honeycomb and auxetic designs [108,115–121], such as the combined re-entrant double-arrow honeycomb [114], exhibit a double-plateau response, confirming the benefit of staged collapse for buffering and energy absorption. However, these reported structures generally remain limited to one or two dominant plateau stages, whereas the CorTube gradient design provides a broader multi-stage plateau response, and the type1 angle-gradient configuration further generates two additional load platforms at 4.76 MPa and 10.72 MPa beyond the first stage. Therefore, the advantage of the CorTube system lies not only in the magnitude of performance enhancement but also in the wider and more programmable load-bearing range enabled by gradient sequencing.

A further distinction emerges when recoverability is considered in Fig. 8(b). Existing 4D-printed and recoverable absorbers, including reversible meta-sandwiches [118], cyclic soft/hard meta-structures [120], and zero-Poisson's-ratio 4D metamaterials [121], have demonstrated shape recovery, hysteretic energy dissipation, and adaptive compressive response under repeated loading. These studies confirm that recoverability can be integrated with energy absorption, but they do not generally emphasize gradient-programmed multi-stage plateau regulation over a broad stress range. In contrast, the CorTube system combines thermal shape recovery with retained early-stage progressive-collapse behavior. The structure can recover its geometry within 5 s after heating, while the linear regime and the first load

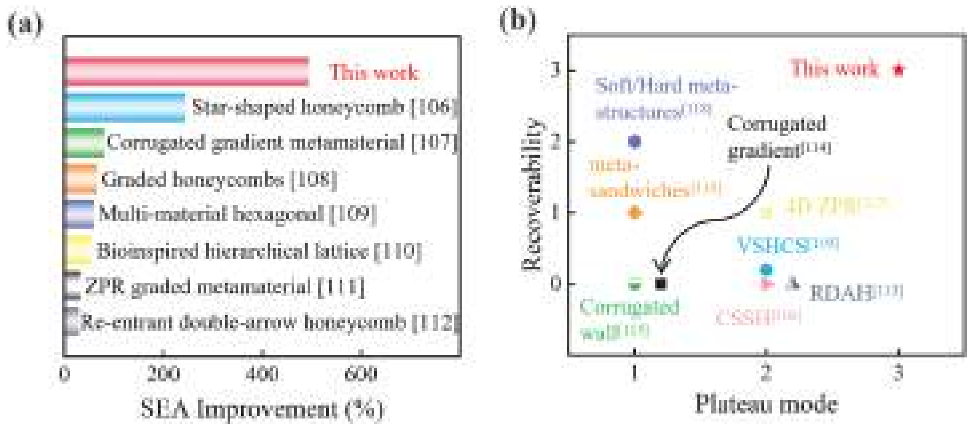

Fig. 8. Comparison of energy-absorption enhancement achieved by representative metamaterial design strategies reported in the literature. The comparison is intended to illustrate the effectiveness of different structural design concepts rather than provide a direct ranking under identical material and testing conditions, (a) Relative improvement in energy-absorption-related performance of representative structures; (b) Comparison of plateau mode and recoverability among representative energy-absorbing structures.

plateau remain highly stable during repeated cycles, and the later plateaus in the first three cycle tests also maintain high consistency. Taken together, these comparisons indicate that the proposed CorTube metamaterial is distinguished not by a single isolated metric, but by the combination of lightweight construction, gradient-controlled multi--stage load regulation, and multi-cycle reusable mechanical response within one unified plate–tube cellular architecture.

It should be noted that the comparisons presented in Fig. 8 are intended to evaluate the effectiveness of different structural design strategies for enhancing energy absorption rather than to establish direct performance rankings among structures fabricated from different materials or tested under different conditions. To minimize the influence of specimen mass, specific energy absorption (SEA) was adopted as the primary comparison metric because it is one of the most widely used mass-normalized indicators in energy-absorbing metamaterials. Nevertheless, differences in constituent materials, relative densities, and loading conditions among published studies should be considered when interpreting the absolute SEA values.

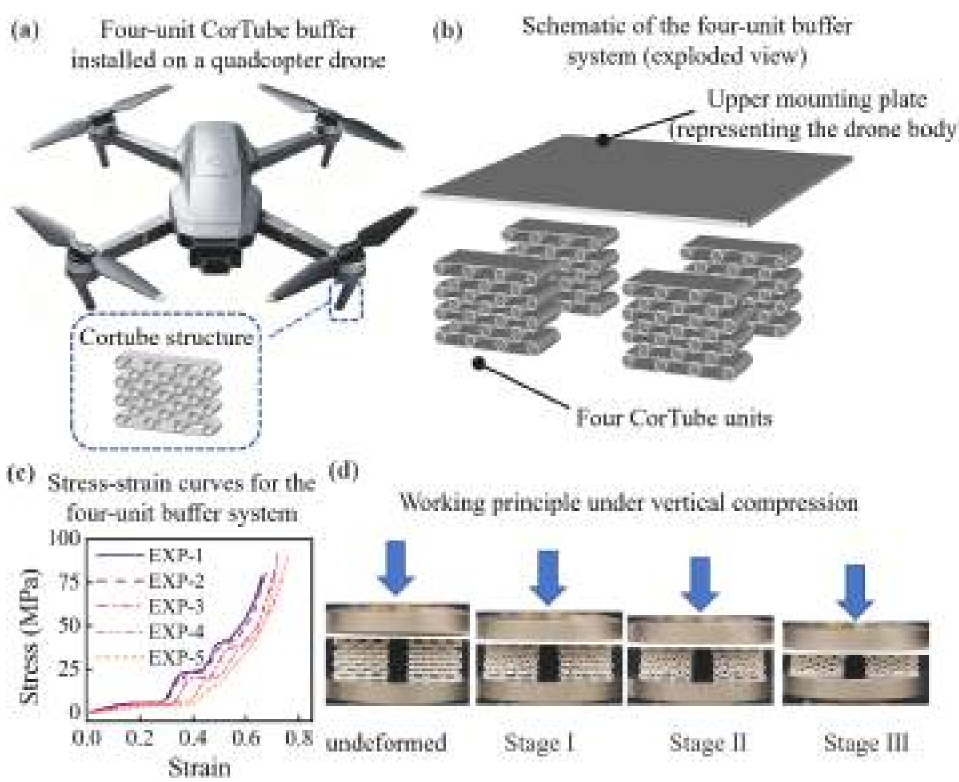

Fig. 9. Scaled UAV landing-buffer prototype based on four identical Type2 CorTube units. (a) Schematic illustration of the four-unit CorTube buffer installed beneath a quadcopter frame, where each CorTube unit serves as an independent landing cushioning element. (b) Structural model of the simplified four-unit buffer, consisting of an upper rigid plate and four type2 angle-gradient CorTube units arranged symmetrically at the four corners. (c) Representative quasi-static compression response of the four-unit buffer. The staged stress–strain curve indicates that the assembled prototype retains the multi-stage load-bearing behavior of the type2 CorTube structure. (d) Optical images of the four-unit buffer during vertical compression, showing progressive deformation from the initial state to Stage I, Stage II, and Stage III. The vertical arrows indicate the applied compressive load.

4.8. Scaled UAV landing-buffer demonstration

To validate the engineering applicability of the developed CorTube metamaterial in practical scenarios, this study designs a scaled UAV landing buffer prototype with four identical type2 angle-gradient CorTube structures (Fig. 9). The type2 configuration is selected primarily for its distinct multi-stage compression response and fast thermal shape recovery performance. For prototype assembly, the four CorTube units are symmetrically installed at four corners of a simplified quadcopter support frame. The upper rigid plate simulates the bottom chassis of the UAV body, while the embedded CorTube units undertake compressive cushioning duties throughout landing movements. This simplified structural model effectively assesses the feasibility of applying the proposed metamaterial to lightweight landing buffer designs.

Quasi-static compression tests are conducted on the prototype under identical loading conditions adopted for single-unit experiments. During the compression process, the upper plate delivers vertical loads to four CorTube units and drives their synchronous deformation. As illustrated in Fig. 9(d), the four-unit buffer retains the unique staged deformation properties of standard type2 CorTube structures. The initial deformation phase relies on bending behaviors and contact state evolution of the corrugated plate-tube composite structure, corresponding to the primary buffering stage. Increased compressive displacement triggers progressive collapse of CorTube units, generates continuous load-bearing phases, and realizes multi-stage energy absorption. These findings prove that the plateau-forming mechanism of individual CorTube structures can be well maintained after integrated assembly into a landing buffer prototype.

Application-oriented compression tests further verify the reliable buffering performance of the proposed structural design. Unlike conventional rigid supports without CorTube cushioning, the four-unit assembly disperses concentrated vertical compression into gradual structural deformation, which suppresses sudden load impact on the upper plate. Furthermore, the parallel arrangement of four CorTube units improves the overall load-bearing capacity of the prototype while preserving the intrinsic staged energy-absorption characteristics of single type2 units. Deformed CorTube units can recover their original geometric morphology under 80 °C thermal stimulation, consistent with the shape-memory recovery principle demonstrated in Section 4.5. The assembled prototype, therefore, demonstrates the great potential of CorTube metamaterials for lightweight, reusable, and load-adaptive UAV landing buffer applications.

This prototype only serves as a scaled quasi-static conceptual verification model, rather than a full-scale UAV landing test platform. Actual UAV landing scenarios involve dynamic impact effects, complex boundary constraints, and random eccentric loading, all of which fall outside the scope of this study. Even so, the experimental results confirm that CorTube units can be embedded into conventional engineering components and produce stable multi-stage compressive buffering via the progressive-collapse mechanism validated in material-level tests. Subsequent research will explore dynamic landing impact experiments, optimized mounting schemes, and multi-material/fiber-reinforced shape-memory CorTube buffers to advance the durability and practicality of the proposed system.

5. Conclusion

In this work, we have pioneered a multi-cycle reusable gradient energy-absorbing metamaterial by combining a corrugated plate-tube (CorTube) architecture with shape-memory PLA and 4D printing. Unlike conventional energy absorbers with fixed post-fabrication responses, the present design uses gradient sequencing to spatially redistribute local activation events, thereby converting relatively concentrated collapse into programmable multi-stage progressive collapse. Experimental and numerical results consistently show that the mechanical roles of the three gradient parameters are distinct: tube spacing primarily controls the onset and stability of the first plateau, corrugation angle mainly governs the collapse sequence and plateau separation, and tube diameter acts mainly as a secondary tuning parameter. In this sense, the main contribution of this work is not merely an increase in absorbed energy, but the establishment of a gradient-enabled design route for stage-wise load regulation in a reusable plate-tube metamaterial system.

This gradient-controlled collapse mechanism leads to clear performance gains. Compared with homogeneous unit structures, the gradient CorTube assemblies broaden the accessible compressive load range by generating multiple load plateaus rather than a single dominant one. The best-performing angle-gradient configuration achieves a total specific energy absorption of 1.088 J/g, corresponding to an increase of 8-fold enhancement relative to the best homogeneous CorTube unit, and further provides two additional load plateaus at 4.76 and 10.72 MPa. These results demonstrate that gradient design can simultaneously enhance cumulative energy absorption and improve load-range adaptability, which is especially valuable for protective and buffering systems subjected to spatially non-uniform or variable loads.

The proposed system also exhibits strong thermal recoverability and partial mechanical reusability. After deformation, the structures recover their original shapes within 5 s under thermal activation, and cyclic compression–recovery tests show that the linear regime and the first load plateau remain highly stable over repeated cycles. However, the later plateau stages progressively deteriorate after being compressed three times, because local damage accumulates in the tube regions, indicating that thermal recovery restores the macroscopic geometry more effectively than the deeper stage-wise collapse mechanism. This observation defines the practical boundary of the present design: the CorTube system is highly effective as a reusable first-stage buffer with additional damage-sensitive reserve absorption capacity, rather than as a perfectly invariant multi-stage absorber over unlimited cycles. Although the employed shape-memory PLA provides excellent printability and rapid thermal recovery, its inherent brittleness may limit long-term cyclic durability. Future studies may explore tougher shape-memory polymers or fiber-reinforced shape-memory composites to further improve service performance.

Overall, this work presents a mechanically validated framework for lightweight, multi-cycle reusable, and load-adaptive metamaterials via gradient architecture and shape-memory reconfiguration. The proposed CorTube metamaterial exhibits excellent linear region and reusability of the first loading plateau over six cycles. The second and third plateaus remain stable in the first three cycles, after which the performance gradually declines. Therefore, the proposed CorTube metamaterials should be considered as limited-cycle reusable energy absorbers. The application demonstration using a quadcopter landing buffer illustrates the practical utility of the gradient CorTube design, showing effective load reduction, staged energy absorption, and recoverable structural geometry after thermal activation.

It is also important to note that, due to the large number of structural configurations investigated (19 designs), repeated compression tests were performed only on two representative samples (the 0° unit and the angle-gradient type2 structure, Fig. S24, S25), which confirmed excellent repeatability. For the remaining configurations, single specimens were tested, which is a common practice in many 3D-printed metamaterial studies involving extensive parametric surveys. Nonetheless, we acknowledge that full statistical replication across all designs would further strengthen the quantitative conclusions, and this should be addressed in future work.

Although the current work is limited to quasi-static uniaxial compression and single-material PLA structures, the underlying design concept can be extended to multi-material 4D printing, dynamic loading, and more advanced optimization strategies. Such developments may further expand the applicability of gradient CorTube metamaterials in reusable impact mitigation, personal protective systems, and other adaptive energy-absorbing devices.

CRediT authorship contribution statement

Zhao Peng: Writing – review & editing, Writing – original draft, Visualization, Validation, Methodology, Formal analysis, Data curation, Conceptualization. **Chengjun Zeng:** Writing – review & editing, Methodology. **Wei Zhao:** Writing – review & editing, Supervision, Methodology, Conceptualization. **Jinsong Leng:** Supervision, Funding acquisition. **Yanju Liu:** Supervision, Resources, Funding acquisition.

Declaration of competing interest

The authors declare that they have no known competing financial interests or personal relationships that could have appeared to influence the work reported in this paper.

Acknowledgments

This work is supported by the National Natural Science Foundation of China (Grant No. 92271206, 12472147, 12402160), the Research Fund of State Key Laboratory of Mechanics and Control for Aerospace Structures (Nanjing University of Aeronautics and astronautics) (Grant No. MCAS-E- 0224G02), China Postdoctoral Science Foundation (Grant No. 2022M720962, 2023T160167), and The "New Era Outstanding Master's and Doctoral Theses of Longjiang" Funding Project, LJYXL2022-051.

Supplementary materials

Supplementary material associated with this article can be found, in the online version, at doi:10.1016/j.ijmecsci.2026.111885.

Appendix A. Structural parameters of the unit and gradient structures

Table A1
Structural parameters of the unit and gradient structures.

Sample	angle(°)	L(mm)	D(mm)
0	0	27	5
5	15	27	5
10	10	27	5
15	15	27	5
d27	0	27	5
d31	0	31	5
d35	0	35	5
D4	15	27	4
D5	15	27	5
D6	15	27	6
The following are the gradient structures			
type1	15-10-5-0-15-10-5-0	27	5
type2	0-5-10-15-15-10-5-0	27	5
type3	15-10-5-0-0-5-10-15	27	5
type4	0	27-31-35-35-31-27	5
type5	0	35-31-27-27-31-35	5
type6	0	35-31-27-35-31-27	5
type7	15	27	6-5-4-4-5-6
type8	15	27	4-5-6-4-5-6
type9	15	27	4-5-6-6-5-4

Appendix B. Parameters of the applied constitutive model:

Table B1
Parameters of the applied constitutive model.

Description	Parameter	Values
Hyperelastic parameters	C_{10},	393.958 MPa,
	D_1	0.0006443 MPa^{-1}
Thermal expansion coefficient	a	0.00017(at 40 °C)
WLF reference temperature	T_0	35 °C
WLF constant	C_1	4.5
WLF constant	C_2	55

Appendix C. Vertical compression FEA model of CorTube structure:

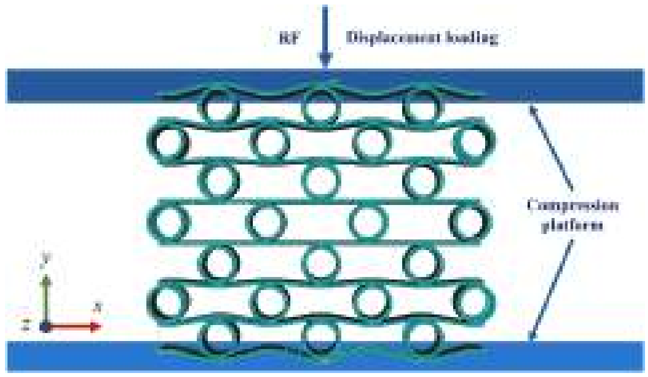

Fig. C1. Vertical compression finite element model of CorTube structure, where the upper and lower blue planes are loading platforms. The lower platform is fixed and the upper platform applies a displacement load.

Appendix D. Compression test of CorTube units:

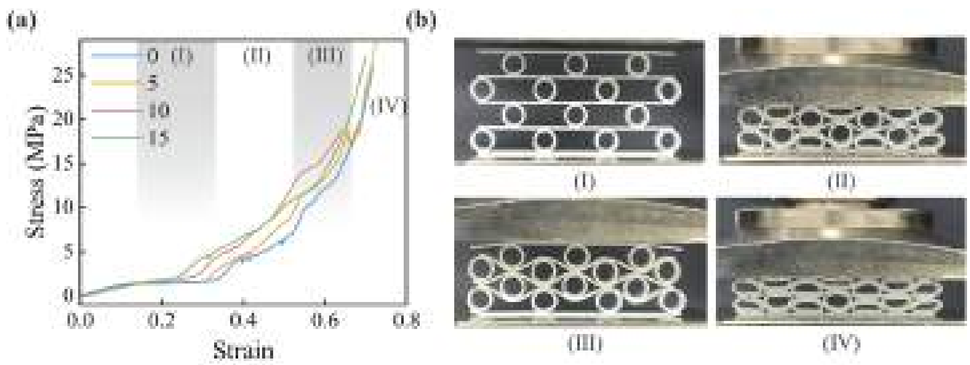

Fig. D1. Compression test of CorTube units with different corrugated plate angles, its stress-strain curve can be divided into 4 stages: (I) first load platform stage; (II) second compression stage; (III) third compression stage; (IV) densification stage: (a) structural compression experiment stress-strain curve, (b) Compression optical image of the structure with a corrugated plate angle of 0°.

Appendix E. Shape recovery process of CorTube structures:

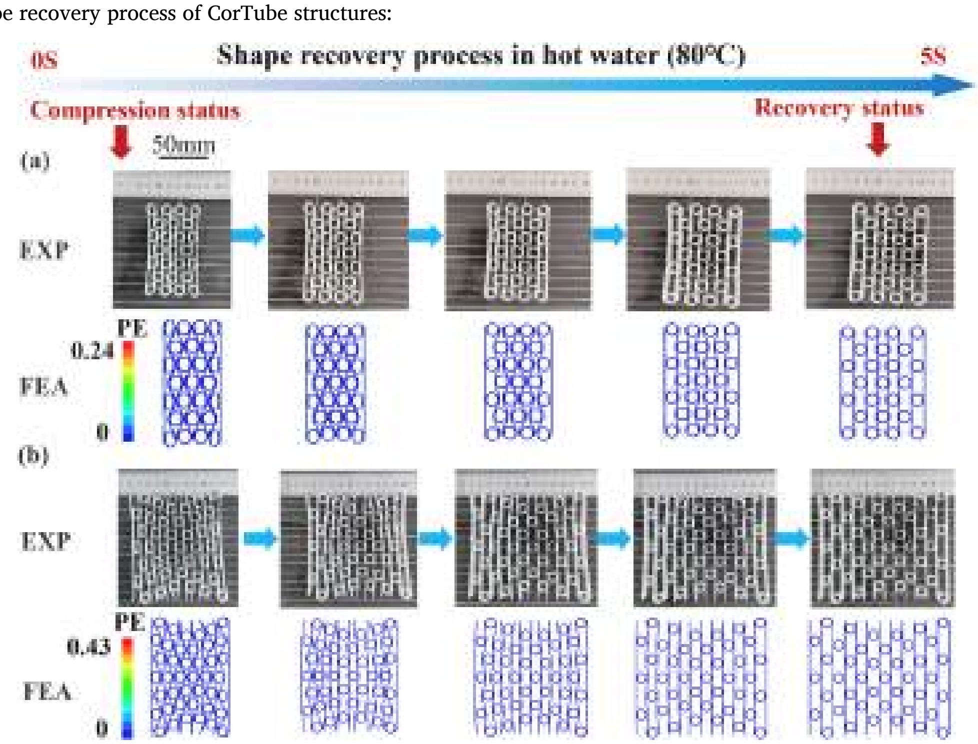

Fig. E1. Shape recovery in experiment and FE analysis of two CorTube gradient structures (PE: Plastic strain). From left to right are images of the CorTube gradient structures at different time points, from 0 s to 5 s after thermal stimulation. The CorTube gradient structures gradually recover their original shapes from the compressed state. In each subfigure, the upper part shows the experimental results, while the lower part displays the simulation (FE analysis) results. (a) type2 gradient structure shape recovery process; (b) type5 gradient structure shape recovery process.

Appendix F. Comparison of compressive modulus before and after cyclic compression:

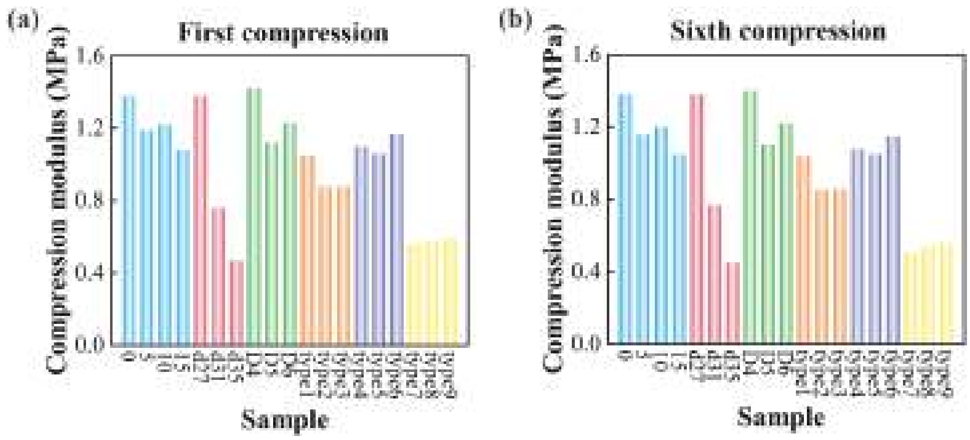

Fig. F1. Compression modulus of the structures in the linear stage. The results of the sixth compression test are nearly identical to those of the first compression test. (a) The first compression result of the CorTube structures, (b) the sixth compression result of the CorTube structures.

Data availability

Data will be made available on request.

References

[1] Zhou X, Ren L. Advances in 3D/4D printing of mechanical metamaterials: from manufacturing to applications. Compos B: Eng 2023;254:110585. https://doi.org/10.1016/j.compositesb.2023.110585.

[2] Surjadi JU, Gao L, Du H, et al. Mechanical metamaterials and their engineering applications. Adv Eng Mater 2019;21(3):1800864. https://doi.org/10.1002/adem.201800864.

[3] Carton M, Kowalewski JF, Guo J, et al. Bridging hard and soft: mechanical metamaterials enable rigid torque transmission in soft robots. Sci Robot 2025;10 (100):eads0548. https://doi.org/10.1126/scirobotics.ads0548.

[4] Sun M, Qiu Z, Chen Q, et al. Mechanical properties of a novel mechanical metamaterial with multi-stable and mono-stable characteristics. Thin-Walled Struct 2025;212:113230. https://doi.org/10.1016/j.tws.2025.113230.

[5] Uddin KZ, Heras M, Youssef G, et al. Multiscale experimental characterization of nonlinear mechanics and auxeticity in mechanical metamaterials with rotating squares. Compos Struct 2025;357:118931. https://doi.org/10.1016/j.compstruct.2025.118931.

[6] Wei Y, Pan F, Lin X, et al. On-demand reprogrammable mechanical metamaterial driven by structure performance relations. Adv Mater 2025;37(9):2410865. https://doi.org/10.1002/adma.202410865.

[7] Li D, Gao R, Dong L, et al. A novel 3D re-entrant unit cell structure with negative Poisson's ratio and tunable stiffness. Smart Mater Struct 2020;29(4):045015. https://doi.org/10.1088/1361-665X/ab6696.

[8] Wang L, Chen Z, Cheng L. A metamaterial plate with magnetorheological elastomers and gradient resonators for tuneable, low-frequency and broadband flexural wave manipulation. Thin-Walled Struct 2023;184:110521. https://doi.org/10.1016/j.tws.2022.110521.

[9] Dey S, Fan C, Gothelf KV, origami DNA, et al. Nat Rev Methods Primers 2021;1 (1):1–24. https://doi.org/10.1038/s43586-020-00009-8.

[10] Barri K, Zhang Q, Swink I, et al. Patient-specific self-powered metamaterial implants for detecting bone healing progress. Adv Funct Mater 2022;32(32): 2203533. https://doi.org/10.1002/adfm.202203533.

[11] Kazim M, Pal A, Goswami D. Mechanical metamaterials for bioengineering. Vitro, wearable, and implantable applications. adv eng mater, 27; 2025, 2401806. https://doi.org/10.1002/adem.202401806.

[12] Xin X, Liu L, Liu Y, et al. 4D Printing auxetic metamaterials with tunable, programmable, and reconfigurable mechanical properties. Adv Funct Mater 2020; 30(43):2004226. https://doi.org/10.1002/adfm.202004226.

[13] Bagci F, Gulsu MS, Akaoglu B. Dual-band measurement of complex permittivity in a microwave waveguide with a flexible, thin and sensitive metamaterial-based sensor. Sens Actuators Phys 2022;338:113480. https://doi.org/10.1016/j.sna.2022.113480.

[14] Pyo S, Park K. Mechanical metamaterials for sensor and actuator applications. Int J Pr Eng Man-gt 2024;11(1):291–320. https://doi.org/10.1007/s40684-023-00549-w.

[15] Barri K, Jiao P, Zhang Q. Multifunctional meta-tribomaterial nanogenerators for energy harvesting and active sensing. Nano Energy 2021;86:106074. https://doi.org/10.1016/j.nanoen.2021.106074.

[16] Liao G, Luan C, Wang Z, et al. Acoustic metamaterials: a review of theories, structures, fabrication approaches, and applications. Adv Mater Technol 2021;6 (5):2000787. https://doi.org/10.1002/admt.202000787.

[17] Yoon G, Kim I, Rho J. Challenges in fabrication towards realization of practical metamaterials. Microelectron Eng 2016;163:7–20. https://doi.org/10.1016/j.mee.2016.05.005.

[18] Walia S, Shah CM, Gutruf P, et al. Flexible metasurfaces and metamaterials: a review of materials and fabrication processes at micro- and nano-scales. Appl Phys Rev 2015;2(1):011303. https://doi.org/10.1063/1.4913751.

[19] Mizzi L, Salvati E, Spaggiari A, et al. Highly stretchable two-dimensional auxetic metamaterial sheets fabricated *via* direct-laser cutting. Int J Mech Sci 2020;167: 105242. https://doi.org/10.1016/j.ijmecsci.2019.105242.

[20] Yuan X, Chen M, Yao Y, et al. Recent progress in the design and fabrication of multifunctional structures based on metamaterials. Curr Opin Solid St M 2021;25 (1):100883. https://doi.org/10.1016/j.cossms.2020.100883.

[21] Almesmari A, Baghous N, Ejeh CJ, et al. Review of additively manufactured polymeric metamaterials: design, fabrication, testing and modeling. Polym (Basel) 2023;15(19):3858. https://doi.org/10.3390/polym15193858.

[22] Pahlavani H, Tsifoutis-Kazolis K, Saldivar MC, et al. Deep learning for size-agnostic inverse design of random-network 3D printed mechanical metamaterials. Adv Mater 2024;36(6):2303481. https://doi.org/10.1002/adma.202303481.

[23] Salari-Sharif L, Schaedler TA, Valdevit L. Energy dissipation mechanisms in hollow metallic microlattices. J Mater Res 2014;29(16):1755–70. https://doi.org/10.1557/jmr.2014.226.

[24] Liu Y, Schaedler TA, Jacobsen AJ, et al. Quasi-static energy absorption of hollow microlattice structures. Compos B: Eng 2014;77:1–13. https://doi.org/10.1016/j.mechmat.2014.06.008.

[25] Lee D, Song J, Min K, et al. Investigating the compressive behavior of zeolite-based porous mechanical metamaterials. Mater Des 2025;249:113541. https://doi.org/10.1016/j.matdes.2024.113541.

[26] He Y, Bi Z, Wang T, et al. Design and mechanical properties analysis of hexagonal perforated honeycomb metamaterial. Int J Mech Sci 2024;270:109091. https://doi.org/10.1016/j.ijmecsci.2024.109091.

[27] Ma N, Han S, Han Q, et al. Design and compressive behaviors of the gradient re-entrant origami honeycomb metamaterials. Thin-Walled Struct 2024;198: 111652. https://doi.org/10.1016/j.tws.2024.111652.

[28] Yang H, Zhang J, Wang J, et al. Delocalized deformation enhanced reusable energy absorption metamaterials based on bistable tensegrity. Adv Funct Mater 2025;35(5):2410217. https://doi.org/10.1002/adfm.202410217.

[29] Pham MS, Liu C, Todd I, et al. Damage-tolerant architected materials inspired by crystal microstructure. Nature 2019;565(7739):305–11. https://doi.org/10.1038/s41586-018-0850-3.

[30] Shaikeea AJD, Cui H, O'Masta M, et al. The toughness of mechanical metamaterials. Nat Mater 2022;21(3):297–304. https://doi.org/10.1038/s41563-021-01182-1.

[31] Foster L, Peketi P, Allen T, et al. Application of auxetic foam in sports helmets. Appl Sci 2018;8(3):354.

[32] Lin C, Nicaise SM, Lilley DE, et al. Nanocardboard as a nanoscale analog of hollow sandwich plates. Nat Commun 2018;9(1):4442. https://doi.org/10.1038/s41467-018-06818-6.

[33] Guo H, Zhang J. Performance-oriented and deformation-constrained dual-topology metamaterial with high-stress uniformity and extraordinary plastic property. Adv Mater 2025;37(7):2412064. https://doi.org/10.1002/adma.202412064.

[34] Wu L, Wang Y, Chuang K, et al. A brief review of dynamic mechanical metamaterials for mechanical energy manipulation. Mater Today 2021;44: 168–93. https://doi.org/10.1016/j.mattod.2020.10.006.
[35] Wilt JK, Yang C, Gu GX. Accelerating auxetic metamaterial design with Deep learning. Adv Eng Mater 2020;22(5):1901266. https://doi.org/10.1002/adem.201901266.
[36] Surendranath H, Bruck HA, Gowrisankaran S. Enhancing the optimization of material distributions in Compos Struct using gradient architectures. Int J Solids Struct 2003;40(12):2999–3020. https://doi.org/10.1016/S0020-7683(03)00090-8.
[37] Kuang X, Wu J, Chen K, et al. Grayscale digital light processing 3D printing for highly functionally graded materials. Sci Adv 2019;5(5):eaav5790. https://doi.org/10.1126/sciadv.aav5790.
[38] Zhang P, Qi D, Xue R, et al. Mechanical design and energy absorption performances of rational gradient lattice metamaterials. Compos Struct 2021;277: 114606. https://doi.org/10.1016/j.compstruct.2021.114606.
[39] Surjadi JU, Gao L, Du H, et al. Mechanical metamaterials and their engineering applications. Adv Eng Mater 2019;21(3):1800864. https://doi.org/10.1002/adem.201800864.
[40] Tan X, Chen S, Wang B, et al. Real-time tunable negative stiffness mechanical metamaterial. Extreme Mech Lett 2020;41:100990. https://doi.org/10.1016/j.eml.2020.100990.
[41] Nasim M, Hasan Md J, Galvanetto U. Impact behavior of energy absorbing helmet liners with PA12 lattice structures: a computational study. Int J Mech Sci 2022; 233:107673. https://doi.org/10.1016/j.ijmecsci.2022.107673.
[42] Mustafa Al-Areqi A, Aloyaydi B, Sivasankaran S, et al. Development of 3D printed biodegradable poly-lactic acid/polyurethane foams/milled glass fibers of sustainable composites with application on helmet. Fibers Polym 2023;24(6): 2065–82. https://doi.org/10.1007/s12221-023-00189-6.
[43] Leng B, Ruan D, Tse KM. Recent bicycle helmet designs and directions for future research: a comprehensive review from material and structural mechanics aspects. Int J Impact Eng 2022;168:104317. https://doi.org/10.1016/j.ijimpeng.2022.104317.
[44] Singh O, Behera BK. Review: a developmental perspective on protective helmets. J Mater Sci 2023;58(15):6444–73. https://doi.org/10.1007/s10853-023-08441-3.
[45] Xue S, Xu W, Wang C, et al. Investigation on shock wave mitigation performance of modified polyurea coated helmet. Thin-Walled Struct 2024;198:111704. https://doi.org/10.1016/j.tws.2024.111704.
[46] Wu J, Yang F, Li L, et al. Multi-feature bionic gradient hierarchical lattice metamaterials with multi-synergistic crushing mechanisms. Int J Mech Sci 2024; 283:109383. https://doi.org/10.1016/j.ijmecsci.2024.109383.
[47] Liu Z, Zhu Y, Jiao, et al. Enhanced protective role in materials with gradient structural orientations: lessons from Nature. Acta Biomater 2016;44:31–40. https://doi.org/10.1016/j.actbio.2016.08.005.
[48] Patek SN. Latch-mediated spring actuation (LaMSA): the power of integrated biomechanical systems. J Exp Biol 2023;226(Suppl_1):jeb245262. https://doi.org/10.1242/jeb.245262.
[49] Hyun NP, Olberding JP, De A, et al. Spring and latch dynamics can act as control pathways in ultrafast systems. Bioinspir Biomim 2023;18(2):026002. https://doi.org/10.1088/1748-3190/acaa7c.
[50] Pragya A, Ghosh TK. Soft functionally gradient materials and structures – Natural and manmade: a review. Adv Mater 2023;35(49):2300912. https://doi.org/10.1002/adma.202300912.
[51] Hong C, Li H, Xiong Z, et al. Review of connections for engineered bamboo structures. J Build Eng 2020;30:101324. https://doi.org/10.1016/j.jobe.2020.101324.
[52] Tan T, Rahbar N, Allameh SM, et al. Mechanical properties of functionally graded hierarchical bamboo structures. Acta Biomater 2011;7(10):3796–803. https://doi.org/10.1016/j.actbio.2011.06.008.
[53] Song JF, Xu SC, Wang HX, et al. Bionic design and multi-objective optimization for variable wall thickness tube inspired bamboo structures. Thin-Walled Struct 2018;125:76–88. https://doi.org/10.1016/j.tws.2018.01.010.
[54] Yang K, Hu X, Pan F, et al. An on-demand tunable energy absorption system to resolve multi-directional impacts. Int J Solids Struct 2023;271-272:112257. https://doi.org/10.1016/j.ijsolstr.2023.112257.
[55] Yang K, Rao L, Hu L, et al. Flexible, efficient and adaptive modular impact-resistant metamaterials. Int J Mech Sci 2023;239:107893. https://doi.org/10.1016/j.ijmecsci.2022.107893.
[56] Yang K, Li Z, Huang P, et al. Mechanical and failure characteristics of novel tailorable architected metamaterials against crash impact. Eng Fail Anal 2024; 159:108141. https://doi.org/10.1016/j.engfailanal.2024.108141.
[57] Parandoush P, Zhou C, Lin D. 3D Printing of ultrahigh strength continuous carbon Fiber composites. Adv Eng Mater 2019;21(2):1800622. https://doi.org/10.1002/adem.201800622.
[58] Zeng Q, Zhao Z, Lei H, et al. A deep learning approach for inverse design of gradient mechanical metamaterials. Int J Mech Sci 2023;240:107920. https://doi.org/10.1016/j.ijmecsci.2022.107920.
[59] Lu X, Ambulo CP, Wang S, et al. 4D-Printing of photoswitchable actuators. Angew Chem Int Ed 2021;60(10):5536–43. https://doi.org/10.1002/anie.202012618.
[60] Qi J, Chen Z, Jiang P, et al. Recent progress in active mechanical metamaterials and construction principles. Adv Sci 2022;9(1):2102662. https://doi.org/10.1002/advs.202102662.
[61] Chen T, Pauly M, Reis PM. A reprogrammable mechanical metamaterial with stable memory. Nature 2021;589(7842):386–90. https://doi.org/10.1038/s41586-020-03123-5.
[62] Liu W, Liu H, Cheng Z, He H, Kan Q, Kang G. Prediction of low-velocity impact responses for bio-inspired helicoidal laminates based on machine learning. Int J Impact Eng 2025;195:105144. https://doi.org/10.1016/j.ijimpeng.2024.105144.
[63] Fu K, Zhao Z, Jin L. Programmable granular metamaterials for reusable energy absorption. Adv Funct Mater 2019;29(32):1901258. https://doi.org/10.1002/adfm.201901258.
[64] Pechac JE, Frazier MJ. Metamaterial design strategy for mechanical energy absorption under general loading. Extreme Mech Lett 2022;51:101580. https://doi.org/10.1016/j.eml.2021.101580.
[65] Zhao W, Yue C, Liu L. Mechanical behavior analyses of 4D printed metamaterials structures with excellent energy absorption ability. Compos Struct 2023;304: 116360. https://doi.org/10.1016/j.compstruct.2022.116360.
[66] Wu Z, Zhu B, Wang R, et al. Design of mechanical metamaterial for energy absorption using a beam with a variable cross-section. Mech Mach Theory 2022; 176:105027. https://doi.org/10.1016/j.mechmachtheory.2022.105027.
[67] Zhang H, Chen P, Lin G, et al. A corrugated gradient mechanical metamaterial: lightweight, tunable auxeticity and enhanced specific energy absorption. Thin-Walled Struct 2022;176:109355. https://doi.org/10.1016/j.tws.2022.109355.
[68] Lin H-B, Liu H-T. Load carrying capacity analysis and gradient design of new 3D zero Poisson's ratio structures. Mater Today Commun 2023;36:106915. https://doi.org/10.1016/j.mtcomm.2023.106915.
[69] Nian Y, Wan S, Avcar M, et al. 3D printing functionally graded metamaterial structure: design, fabrication, reinforcement, optimization. Int J Mech Sci 2023; 258:108580. https://doi.org/10.1016/j.ijmecsci.2023.108580.
[70] Hou W, He P, Yang Y, Sang L. Crashworthiness optimization of crash box with 3D-printed lattice structures. Int J Mech Sci 2023;247:108198. https://doi.org/10.1016/j.ijmecsci.2023.108198.
[71] Wu Z, Pan H, Huang P, et al. Biomimetic mechanical robust cement-resin composites with machine learning-assisted gradient hierarchical structures. Adv Mater 2024;36(35):2405183. https://doi.org/10.1002/adma.202405183.
[72] Daynes S, Feih S. Functionally graded lattice structures with tailored stiffness and energy absorption. Int J Mech Sci 2025;285:109861. https://doi.org/10.1016/j.ijmecsci.2024.109861.
[73] Zhang Z, Hu H, Liu S, et al. Study of an auxetic structure made of tubes and corrugated sheets. Phys Status Solidi (b) 2013;250(10):1996–2001. https://doi.org/10.1002/pssb.201248349.
[74] Li ZY, Wang XT, Ma L, et al. Study on the mechanical properties of CFRP composite auxetic structures consist of corrugated sheets and tubes. Compos Struct 2022;292:115655. https://doi.org/10.1016/j.compstruct.2022.115655.
[75] Zeng C, Liu L, Hu Y, et al. Stair-stepping mechanical metamaterials with programmable load plateaus. Adv Funct Mater 2024;34(49):2408887. https://doi.org/10.1002/adfm.202408887.
[76] Liu T, Zhou T, Yao Y, Zhang F, Liu L, Liu Y, et al. Stimulus methods of multi-functional shape memory polymer nanocomposites: a review. Compos A: Appl Sci Manuf 2017;100:20–30. https://doi.org/10.1016/j.compositesa.2017.04.022.
[77] Jin F, Wang F, Guo P, Lyu M, Wang L, Gao D, et al. 4D printing of continuous carbon fiber reinforced composites with magneto-/electro-induced shape memory effect. Chem Eng J 2025;508:160450. https://doi.org/10.1016/j.cej.2025.160450.
[78] Bodaghi M, Wang L, Zhang F, et al. 4D printing roadmap. Smart Mater Struct 2024;33(11):113501. https://doi.org/10.1088/1361-665X/ad5c22.
[79] Yousefi MA, Rahmatabadi D, Baniassadi M, et al. 4D Printing of multifunctional and biodegradable PLA-PBAT-Fe3O4 nanocomposites with supreme mechanical and shape memory properties. Macromol Rapid Commun 2025;46(2):2400661. https://doi.org/10.1002/marc.202400661.
[80] Han D, Morde RS, Mariani S, et al. 4D Printing of a bioinspired microneedle array with backward-facing barbs for enhanced tissue adhesion. Adv Funct Mater 2020; 30(11):1909197. https://doi.org/10.1002/adfm.201909197.
[81] Rahmatabadi D, Soltanmohammadi K, Aberoumand M, et al. 4D printing of porous PLA-TPU structures: effect of applied deformation, loading mode and infill pattern on the shape memory performance. Phys Scr 2024;99(2):025013. https://doi.org/10.1088/1402-4896/ad1957.
[82] Faber JA, Arrieta AF, Studart AR. Bioinspired spring origami. Science 2018;359 (6382):1386–91. https://doi.org/10.1126/science.aap7753.
[83] Saed MO, Ambulo CP, Kim H, et al. Molecularly-engineered, 4D-printed liquid crystal elastomer actuators. Adv Funct Mater 2019;29(3):1806412. https://doi.org/10.1002/adfm.201806412.
[84] Zhang K, Ji J, Kang X, Guo X. Electrothermally actuated network metamaterials with reconfigurable bending deformation modes. Extreme Mech Lett 2024;72: 102241. https://doi.org/10.1016/j.eml.2024.102241.
[85] Ahmed A, Arya S, Gupta V, et al. 4D printing: fundamentals, materials, applications and challenges. Polym (Guildf) 2021;228:123926. https://doi.org/10.1016/j.polymer.2021.123926.
[86] Bhatia A, Sehgal AK. Additive manufacturing materials, methods and applications: a review. Mater Today: Proc 2023;81:1060–7. https://doi.org/10.1016/j.matpr.2021.04.379.
[87] Zhao W, Zeng C, Liu L, et al. Shape memory sandwich structure with reprogrammable shape and mechanical properties. Compos Struct 2025;351: 118604. https://doi.org/10.1016/j.compstruct.2024.118604.
[88] Luo L, Zhang F, Wang L, et al. Recent advances in shape memory polymers: multifunctional materials, multiscale structures, and applications. Adv Funct Mater 2024;34(14):2312036. https://doi.org/10.1002/adfm.202312036.
[89] Lin L, Yan J, Qiu S. Programming the deformation of the temperature driven spiral structure in 4D printing. Smart Mater Struct 2024;33(10):105022. https://doi.org/10.1088/1361-665X/ad7801.

[90] Zhang D, Li M, Qiu N, et al. 4D-printed reusable metamaterial via shape memory effect for energy dissipation. Int J Mech Sci 2024;275:109309. https://doi.org/10.1016/j.ijmecsci.2024.109309.
[91] Dong K, Wang Y, Wang Z, et al. Reusability and energy absorption behavior of 4D printed continuous fiber-reinforced auxetic compos Struct. Compos Appl Sci Manuf 2023;169:107529. https://doi.org/10.1016/j.compositesa.2023.107529.
[92] Zhang X, Han Y, Zhu M, et al. Bio-inspired 4D printed intelligent lattice metamaterials with tunable mechanical property. Int J Mech Sci 2024;272: 109198. https://doi.org/10.1016/j.ijmecsci.2024.109198.
[93] Li ZY, Zhang WM, Zou S, et al. Quasi-static uniaxial compression and low-velocity impact properties of composite auxetic CorTube structure. Thin-Walled Struct 2024;202:112059. https://doi.org/10.1016/j.tws.2024.112059.
[94] Zeng C, Liu L, Zhao W, et al. Mechanical properties and shape memory behavior of 4D printed functionally graded cellular structures. Sci China Technol Sc 2023; 66(12):3522–33. https://doi.org/10.1007/s11431-023-2475-3.
[95] Lin C, Xin X, Tian L, Zhang D, Liu L, Liu Y, et al. Thermal-, magnetic-, and light-responsive 4D printed SMP composites with multiple shape memory effects and their promising applications. Compos B: Eng 2024;274:111257. https://doi.org/10.1016/j.compositesb.2024.111257.
[96] Zhao W, Zeng C, Liu L, Leng J, Liu Y. Shape memory sandwich structure with reprogrammable shape and mechanical properties. Compos Struct 2025;351: 118604. https://doi.org/10.1016/j.compstruct.2024.118604.
[97] Avalle M, Belingardi G, Montanini R. Characterization of polymeric structural foams under compressive impact loading by means of energy-absorption diagram. Int J Impact Eng 2001;25(5):455–72. https://doi.org/10.1016/S0734-743X(00)00060-9.
[98] Sun Y, Li QM. Dynamic compressive behaviour of cellular materials: a review of phenomenon, mechanism and modelling. Int J Impact Eng 2018;112:74–115. https://doi.org/10.1016/j.ijimpeng.2017.10.006.
[99] Quey R, Dawson PR, Barbe F. Large-scale 3D random polycrystals for the finite element method: generation, meshing and remeshing. Comput Methods Appl Mech Eng 2011;200(17):1729–45. https://doi.org/10.1016/j.cma.2011.01.002.
[100] Yang Z, Mei J, Yang M, et al. Membrane-type acoustic metamaterial with negative dynamic mass. Phys Rev Lett 2008;101(20):204301. https://doi.org/10.1103/PhysRevLett.101.204301.
[101] Isleem HF, Qiong T, Chukka NDKR, et al. Machine learning and nonlinear finite element analysis of fiber-reinforced polymer-confined concrete-steel double-skin tubular columns under axial compression. Struct Concr 2025;26(1):248–92. https://doi.org/10.1002/suco.202300835.
[102] Flanagan DP, Belytschko T. A uniform strain hexahedron and quadrilateral with orthogonal hourglass control. Int J Numer Meth Eng 1981;17(5):679–706. https://doi.org/10.1002/nme.1620170504.
[103] Joldes GR, Wittek A, Miller K. An efficient hourglass control implementation for the uniform strain hexahedron using the Total Lagrangian formulation. Commun Numer Methods Eng 2008;24(11):1315–23. https://doi.org/10.1002/cnm.1034.
[104] Zhu S, Tan X, Wang B, et al. Bio-inspired multistable metamaterials with reusable large deformation and ultra-high mechanical performance. Extreme Mech Lett 2019;32:100548. https://doi.org/10.1016/j.eml.2019.100548.
[105] Wang L, Zhu S, Wang B, et al. Latitude-and-longitude-inspired three-dimensional auxetic metamaterials. Extreme Mech Lett 2021;42:101142. https://doi.org/10.1016/j.eml.2020.101142.
[106] Yang L, Harrysson O, West H, et al. Mechanical properties of 3D re-entrant honeycomb auxetic structures realized via additive manufacturing. Int J Solids Struct 2015;69-70:475–90. https://doi.org/10.1016/j.ijsolstr.2015.05.005.
[107] Zhao W, Zhang F, Leng J, et al. Personalized 4D printing of bioinspired tracheal scaffold concept based on magnetic stimulated shape memory composites. Compos Sci Technol 2019;184:107866. https://doi.org/10.1016/j.compscitech.2019.107866.
[108] Li X, Li Z, Guo Z, et al. A novel star-shaped honeycomb with enhanced energy absorption[J]. Compos Struct 2023;309:116716. https://doi.org/10.1016/j.compstruct.2023.116716.
[109] Zhang H, Chen P, Lin G, et al. A corrugated gradient mechanical metamaterial: lightweight, tunable auxeticity and enhanced specific energy absorption[J]. Thin-Walled Struct 2022;176:109355. https://doi.org/10.1016/j.tws.2022.109355.
[110] Gao Y, Chen X, Wei Y. Graded honeycombs with high impact resistance through machine learning-based optimization[J]. Thin-Walled Struct 2023;188:110794. https://doi.org/10.1016/j.tws.2023.110794.
[111] Günaydin K, Rea C, Kazanci Z. Energy absorption enhancement of additively manufactured hexagonal and re-entrant (auxetic) lattice structures by using multi-material reinforcements[J]. Addit Manuf 2022;59:103076. https://doi.org/10.1016/j.addma.2022.103076.
[112] Wang P, Yang F, Zheng B, et al. Breaking the tradeoffs between different mechanical properties in bioinspired hierarchical lattice metamaterials[J]. Adv Funct Mater 2023;33(45):2305978. https://doi.org/10.1002/adfm.202305978.
[113] Hamzehei R, Zolfagharian A, Dariushi S, et al. 3D-printed bio-inspired zero Poisson's ratio graded metamaterials with high energy absorption performance [J]. Smart Mater Struct 2022;31(3):035001. https://doi.org/10.1088/1361-665X/ac47d6.
[114] Zhang W, Wang H, Lou X, et al. On in-plane crushing behavior of a combined re-entrant double-arrow honeycomb[J]. Thin-Walled Struct 2024;194:111303. https://doi.org/10.1016/j.tws.2023.111303.
[115] Etemadi E, Zamani AMM, Scarpa F, et al. Modified re-entrant auxetic metamaterials with energy absorption enhancement[J]. Mater Today Commun 2024;38:108079. https://doi.org/10.1016/j.mtcomm.2024.108079.
[116] Zhang H, Chen P, Lin G, et al. A corrugated gradient mechanical metamaterial: lightweight, tunable auxeticity and enhanced specific energy absorption[J]. Thin-Walled Struct 2022;176:109355. https://doi.org/10.1016/j.tws.2022.109355.
[117] Wang W, Wu Y, Xu M, et al. Design and optimization of a corrugated tubular shell structure based on triply periodic minimal surface[J]. Structures 2024;64: 106543. https://doi.org/10.1016/j.istruc.2024.106543.
[118] Bodaghi M, Serjouei A, Zolfagharian A, et al. Reversible energy absorbing meta-sandwiches by FDM 4D printing[J]. Int J Mech Sci 2020;173:105451. https://doi.org/10.1016/j.ijmecsci.2020.105451.
[119] Hamzehei R, Serjouei A, Wu N, et al. 4D Metamaterials with zero Poisson's ratio, shape recovery, and energy absorption features[J]. Adv Eng Mater 2022;24(9): 2200656. https://doi.org/10.1002/adem.202270037.
[120] Yousefi A, Jolaiy S, Lalegani DM, et al. 3D-Printed soft and hard meta-structures with supreme energy absorption and dissipation capacities in cyclic loading conditions[J]. Adv Eng Mater 2023;25(4):2201189. https://doi.org/10.1002/adem.202201189.
[121] Zhang X, Hao H, Tian R, et al. Quasi-static compression and dynamic crushing behaviors of novel hybrid re-entrant auxetic metamaterials with enhanced energy-absorption[J]. Compos Struct 2022;288:115399. https://doi.org/10.1016/j.compstruct.2022.115399.